Dispersion and attenuation measurements of the elastic moduli of a dual-porosity limestone

J V M Borgomano, L Pimienta, J Fortin, Y Guéguen

▶ **To cite this version:**

J V M Borgomano, L Pimienta, J Fortin, Y Guéguen. Dispersion and attenuation measurements of the elastic moduli of a dual-porosity limestone. Journal of Geophysical Research : Solid Earth, 2017, 122, pp.2690 - 2711. 10.1002/2016jb013816 . hal-03978448

HAL Id: hal-03978448

https://cnrs.hal.science/hal-03978448

Submitted on 8 Feb 2023

HAL is a multi-disciplinary open access archive for the deposit and dissemination of scientific research documents, whether they are published or not. The documents may come from teaching and research institutions in France or abroad, or from public or private research centers.

L'archive ouverte pluridisciplinaire **HAL**, est destinée au dépôt et à la diffusion de documents scientifiques de niveau recherche, publiés ou non, émanant des établissements d'enseignement et de recherche français ou étrangers, des laboratoires publics ou privés.

AGU PUBLICATIONS

JGR

Journal of Geophysical Research: Solid Earth

RESEARCH ARTICLE
10.1002/2016JB013816

Special Section:
Rock Physics of the Upper Crust

Dispersion and attenuation measurements of the elastic moduli of a dual-porosity limestone

J. V. M. Borgomano[1], L. Pimienta[1], J. Fortin[1], and Y. Guéguen[1]

[1]Laboratoire de Géologie de l'ENS, PSL Research University, Paris, France

Key Points:
- Elastic moduli dispersion and attenuation have been measured on a limestone, using stress-strain oscillations and ultrasonic measurements
- The drained/undrained transition has been measured for all moduli and is consistent with Biot-Gassmann's predictions
- There is no dispersive transition beyond the undrained regime, meaning no squirt flow or local diffusion between the micropores and macropores

Correspondence to:
J. V. M. Borgomano,
borgomano@geologie.ens.fr

Citation:
Borgomano, J. V. M., L. Pimienta, J. Fortin, and Y. Guéguen (2017), Dispersion and attenuation measurements of the elastic moduli of a dual-porosity limestone, *J. Geophys. Res. Solid Earth*, *122*, 2690–2711, doi:10.1002/2016JB013816.

Received 1 DEC 2016
Accepted 26 MAR 2017
Accepted article online 7 APR 2017
Published online 22 APR 2017

©2017. American Geophysical Union. All Rights Reserved.

Abstract The dispersion and the attenuation of the elastic moduli of a Lavoux limestone have been measured over a large frequency range: 10^{-3} Hz to 10^{1} Hz and 1 MHz. The studied sample comes from a Dogger outcrop of Paris Basin and has the particularity to have a bimodal porosity distribution, with an equal proportion of intragranular microporosity and intergranular macroporosity. In addition to ultrasonic measurements, two different stress-strain methods have been used in a triaxial cell to derive all the elastic moduli at various differential pressures. The first method consists of hydrostatic stress oscillations ($f \in [0.004;\ 0.4]$ Hz), using the confining pressure pump, from which the bulk modulus was deduced. The second method consists of axial oscillations ($f \in [0.01;\ 10]$ Hz), using a piezoelectric oscillator on top of the sample, from which Young's modulus and Poisson's ratio were deduced. With the assumption of an isotropic medium, the bulk modulus (K) and the shear modulus (G) can also be computed from the axial oscillations. The sample was studied under dry, glycerin- and water-saturated conditions, in order to scale frequency by the viscosity of the fluid. Results show a dispersion at around 200 Hz for water-saturated conditions, affecting all the moduli except the shear modulus. This dispersion is related to the drained/undrained transition, and the bulk modulus deduced from the axial and hydrostatic oscillations are consistent with each other and with Biot-Gassmann's equations. No dispersion has been detected beyond that frequency. This was interpreted as the absence of squirt flow or local diffusion between the microporous oolites and the macropores.

1. Introduction

In fluid-saturated porous media, the dependence to frequency of the body wave velocities (V_P and V_S) rises questions on how to compare low-frequency field measurements (100 Hz for seismic data and 10 kHz for sonic logs) to conventional high-frequency measurements in the laboratory (1 MHz for ultrasonic). These dispersions in elastic wave velocities are related to the dispersion of the elastic moduli, which can be affected by fluid flows occurring at different scales in the porosity [*Batzle et al.*, 2006; *Muller et al.*, 2010; *Sarout*, 2012].

When the porous medium is submitted to an oscillating stress field, the deformation of the solid frame may induce a fluid pressure variation if the fluid has no time to diffuse through the pore network. In fully saturated conditions, this fluid diffusion can occur at different scales [*Sarout*, 2012]: global within the wavelength scale or local within a representative elementary volume (REV). Local flow, or squirt flow, may equalize the fluid pressure between compliant cracks and rounded pores within one REV [*Mavko and Jizba*, 1991], whereas global flow equalizes pressure through all the connected REVs. Three fluid flow regimes can be considered from this: drained, undrained, and unrelaxed regimes [*Pimienta et al.*, 2016a]. The undrained and unrelaxed regimes refer to, respectively, the saturated isobaric and the saturated isolated regimes described by *O'Connell and Budiansky* [1977]. The drained regime occurs when the fluid has time to diffuse by local and global flow through all the REVs. The elastic properties of the porous medium are similar to dry conditions. Then, when the frequency increases, the fluid stops diffusing at wavelength scale, letting place to the undrained regime. In this regime, the REVs are as disconnected from each other and remain isobaric. Because of the deformation of the frame, the fluid pressure increases in the porosity, therefore increasing the stiffness of the medium. The two previous regimes are well accounted for in quasi-static poroelasticity [*Gassmann*, 1951]. Finally, when the frequency is high enough, pressure may not equilibrate by local flow within the REVs. This is the case, for example, of squirt flow between cracks and stiff pores, leading to the unrelaxed regime [*Dvorkin et al.*, 1995; *Shafiro and Kachanov*, 1997]. In this regime, the fluid can be considered immobile, and higher pressure gradients are

21699356, 2017, 4, Downloaded from https://agupubs.onlinelibrary.wiley.com/doi/10.1002/2016JB013816 by Cochrane France, Wiley Online Library on [08/02/2023]. See the Terms and Conditions (https://onlinelibrary.wiley.com/terms-and-conditions) on Wiley Online Library for rules of use; OA articles are governed by the applicable Creative Commons License

maintained in the cracks. This increases further the stiffness of the medium. Effective medium theories are possible tools to predict the elastic properties in this last regime [e.g., *Adelinet et al.*, 2011].

While the elastic properties are not frequency dependent within a specific regime, they show dispersion and attenuation in the transitions between these regimes [*Pimienta et al.*, 2015a]. The two cutoff frequencies, f_1 and f_2, respectively for the drained/undrained transition and undrained/unrelaxed transition, can be expressed as follows [*O'Connell and Budiansky*, 1977; *Cleary*, 1978]:

$$f_1 = \frac{4kK_d}{\eta L^2} \quad \text{and} \quad f_2 = \frac{K_s \xi^3}{\eta}, \tag{1}$$

where k is the permeability, K_d is the drained bulk modulus, K_s is the skeleton's bulk modulus, ξ the average crack aspect ratio, η the fluid's dynamic viscosity, and L the wavelength. At low frequencies in the laboratory, the corresponding wavelength is generally larger than the sample's length, in which case L is taken equal to the sample's length. When there is dispersion of an elastic modulus M, in other words, when there is viscous dissipation in the fluid, the rheology of the medium is similar to that of a viscoelastic material [*O'Connell and Budiansky*, 1977]. One can measure a phase shift $\Delta\phi$ between the stress and the strain response. The dissipation related to M is usually quantified from the inverse of the quality factor Q_M^{-1}, such that [*O'Connell and Budiansky*, 1978]:

$$Q_M^{-1} = \tan(\Delta\phi). \tag{2}$$

Carbonate rocks are characterized by complex microstructures and heterogeneous pore types [*Lucia*, 1995]. For a given porosity, carbonate rocks were shown to exhibit a wide range of P wave and S wave velocities, due to the large variety of pore types [*Eberli et al.*, 2003]. Their elastic properties are affected by the pore network and the mineralogy, which can be modified through diagenetic processes [*Fournier and Borgomano*, 2009]. Several studies have attempted to understand the relationship between seismic wave velocity and porosity [e.g., *Anselmetti and Eberli*, 1993; *Verwer et al.*, 2010] or to verify the applicability of Biot-Gassmann's fluid substitution theory [e.g., *Baechle et al.*, 2009; *Fabricius et al.*, 2010]. Very few studies aimed at characterizing the dispersion and the attenuation at seismic frequencies in carbonate rocks, due to the interplay between microstructure and fluid flow [e.g., *Adam et al.*, 2006, 2009; *Mikhaltsevitch et al.*, 2016a]. This is, however, essential in hydrocarbon exploration and reservoir characterization, to improve the inversion of the rock properties using seismic data. In this study, we present our first measurements of dispersion and attenuation of the elastic moduli of a pure calcite oolitic limestone from Lavoux (France).

2. Experimental Setup

To measure the dispersion and the attenuation of the elastic moduli over a large frequency range, we used the stress-strain method, combined with ultrasonic measurements, in a triaxial cell at the ENS of Paris (Figure 1) [*Fortin et al.*, 2005, 2014; *Adelinet et al.*, 2010; *David et al.*, 2013]. The detailed experimental protocol and the calibration of the apparatus on standard materials can be found in *Pimienta et al.* [2015a] and *Pimienta et al.* [2015b]. With this apparatus, two types of stress oscillations can be achieved: hydrostatic (Figure 1a) to measure the bulk modulus (K) and axial (Figure 1b) to measure the Young's modulus (E) and the Poisson's ratio (ν). To investigate the effect of the fluid's viscosity, the sample's properties were measured under dry, glycerin-saturated and finally water-saturated conditions. At room temperature (22° C), the viscosity of pure glycerin and water is, respectively, $\eta_{gly} = 1$ Pa s and $\eta_{water} = 10^{-3}$ Pa s [*Segur and Oberstar*, 1951] . We also studied the effect of the boundary conditions on the measured elastic properties, with two different configurations for the drainage system: (1) open (drained conditions) and (2) closed (undrained for the system {*sample* + *dead volumes*}) (Figure 1a). *Pimienta et al.* [2016b] demonstrated that the effect of the dead volumes on the measured properties depends upon the ratio of the storage capacities of the sample and the drainage system. In the drained frequency range, the measured properties would tend to their undrained value if the dead volumes tend to zero. The dead volumes of the closed drainage system (second case) were measured at about $V_d = 3.3$ mL for the top and bottom end platens [*Pimienta et al.*, 2016b]. *Pimienta et al.* [2016b] showed that if the dead volumes are greater than $10V_d$, the measured properties converge to the fully drained values. For our experiments, when the drainage system is open (first case), the dead volumes are in fact much larger and correspond to the volume of all the hydraulic tubings added to the volume of fluid in the Quizix pumps (~60 mL). During the stress oscillations, the pore pressure pumps are shut off, to avoid a fluid-induced response back to the sample.

21699356, 2017, 4, Downloaded from https://agupubs.onlinelibrary.wiley.com/doi/10.1002/2016JB013816 by Cochrane France, Wiley Online Library on [08/02/2023]. See the Terms and Conditions (https://onlinelibrary.wiley.com/terms-and-conditions) on Wiley Online Library for rules of use; OA articles are governed by the applicable Creative Commons License

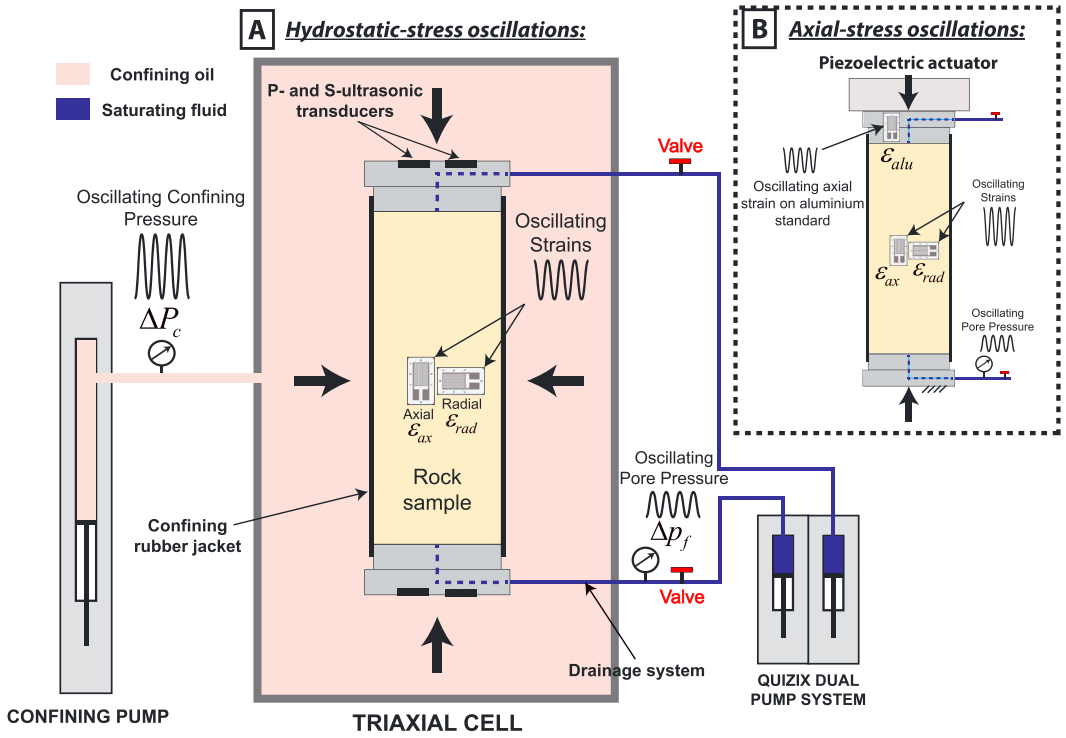

Figure 1. Schematics of the experimental setup for (a) hydrostatic oscillations and (b) axial oscillations, in the triaxial cell at the ENS of Paris. The hydrostatic oscillations were imposed by the confining pump, in the frequency range of [0.004; 0.4] Hz. The axial oscillations were imposed by a piezoelectric actuator mounted over the top end platen, in the frequency range of [0.01; 10] Hz. Strains are measured by axial and radial strain gauges bonded on the sample at midheight. Ultrasonic transducers are settled in the end platens to obtain the *P* and *S* wave velocities at 1 MHz.

The sample is 8 cm long and 4 cm diameter cylinder. To measure the strains, four pairs of 350Ω metal foil strain gauges with axial and radial orientations are glued at midheight all around the lateral surface (Figure 1). Axial strain (ε_{ax}) and radial strain (ε_{rad}) are averaged from all the strain gauges. The sample is under a rubber jacket that separates the pore pressure (p_f) from the confining pressure (P_c) (Figure 1a). When the sample is fluid saturated, the pore pressure is controlled by a Quizix dual pump system connected to the top and bottom of the sample through a drainage circuit (Figure 1a). Throughout all the measurements, the pore pressure was maintained at 2 MPa. Measurements at different differential pressures ($P_{diff} = P_c - p_f$) were done, in a range below the pore-collapse pressure (P^*) of the sample.

2.1. Hydrostatic Stress Oscillations—Bulk Modulus

The hydrostatic stress oscillations give a direct measurement of the bulk modulus K_{hyd} [*Pimienta et al.*, 2015a]. The oscillations are obtained from the confining pressure ΔP_c that oscillates with an amplitude of 0.2 MPa around a mean value P_c (Figure 1a). This amplitude value has been calibrated in order to obtain small strains on the sample ($\varepsilon \sim 10^{-6}$) to remain in the linear elastic domain (Figure 2a) [*Winkler and Murphy*, 1995]. The frequency of these hydrostatic oscillations is between 4×10^{-3} Hz and 4×10^{-1} Hz. The induced volumetric strain signal (ε_{vol}) is calculated by $\varepsilon_{vol} = \varepsilon_{ax} + 2\varepsilon_{rad}$. Thus, the bulk modulus K_{hyd} is obtained from the measured stress ΔP_c and the measured strain ε_{vol} such that

$$K_{hyd} = \frac{-\Delta P_c}{\varepsilon_{vol}}, \tag{3}$$

with the convention $\Delta P_c = -\sigma_{ii}/3$. A linear regression of the stress signal versus the strain signal is then processed to calculate K_{hyd} (Figure 2b).

2.2. Axial Stress Oscillations—Young's Modulus and Poisson's Ratio

In order to perform axial stress oscillations [e.g., *Batzle et al.*, 2006; *Mikhaltsevitch et al.*, 2014; *Tisato and Madonna*, 2012; *Madonna and Tisato*, 2013; *Pimienta et al.*, 2015b; *Szewczyk et al.*, 2016], we used a piezoelectric actuator that is mounted between the axial piston of the triaxial cell and the top end platen (Figure 1b).

21699356, 2017, 4, Downloaded from https://agupubs.onlinelibrary.wiley.com/doi/10.1002/2016JB013816 by Cochrane France, Wiley Online Library on [08/02/2023]. See the Terms and Conditions (https://onlinelibrary.wiley.com/terms-and-conditions) on Wiley Online Library for rules of use; OA articles are governed by the applicable Creative Commons License

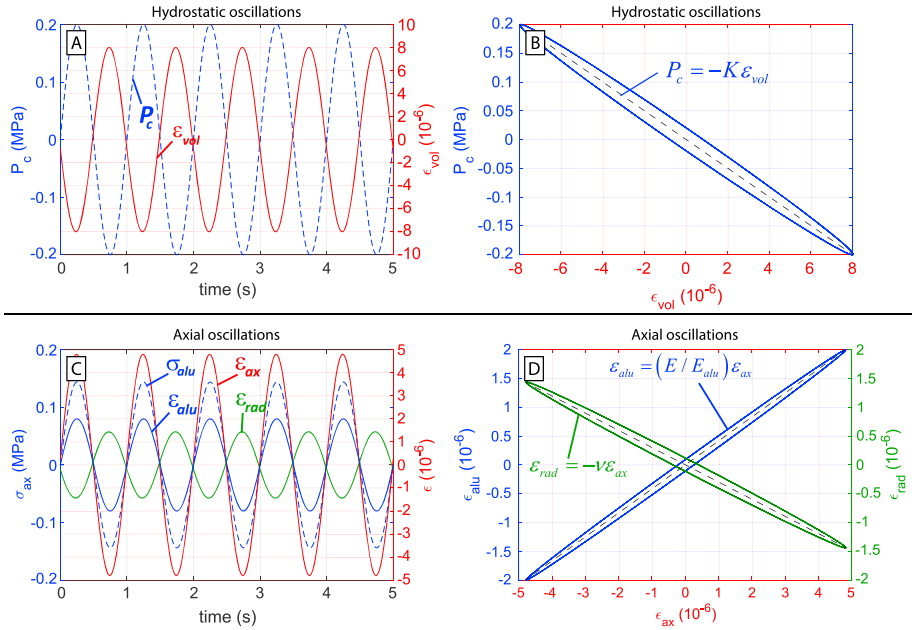

Figure 2. Example of stress and strain versus time recordings during (a, b) hydrostatic oscillations and (c, d) axial oscillations. The elastic moduli are calculated from the linear regressions of the stress versus strain curves (Figures 2b–2d). The ellipse shapes (hysteresis) result from the phase shift between stress and strain when dispersion occurs, similarly to viscoelastic materials.

A small deviatoric stress of 1 MPa is maintained on the assemblage in order to have a good contact. The frequency range of the oscillations applied on the Lavoux sample is 10^{-2} Hz to 10 Hz. The top end platen is made out of AU4G aluminum and is bonded with two axial strain gauges acting as a axial stress sensor (Figure 1b). During the measurements, the two axial strains are averaged (ε_{alu}) and the axial stress is computed from $\sigma_{ax} = E_{alu}.\varepsilon_{alu}$ (Figure 2c), where E_{alu} is the Young's modulus of AU4G (E_{alu}=72 GPa). With the measurements of the axial strain (ε_{ax}) and the radial strain (ε_{rad}) of the sample (Figure 2c), we can directly obtain the Young's modulus (E) and the Poisson's ratio (ν) of the sample:

$$E = \frac{\sigma_{ax}}{\varepsilon_{ax}} \quad \text{and} \quad \nu = -\frac{\varepsilon_{rad}}{\varepsilon_{ax}}. \tag{4}$$

E and ν are determined by linear regression of the signals, respectively, σ_{ax} over ε_{ax} and $-\varepsilon_{rad}$ over ε_{ax} (Figure 2d). A bulk modulus (K_{ax}) and a shear modulus (G_{ax}) are calculated, with the assumption of an isotropic medium:

$$K_{ax} = \frac{E}{3(1-2\nu)} \quad \text{and} \quad G_{ax} = \frac{E}{2(1+\nu)}. \tag{5}$$

K_{ax} can then be compared to the bulk modulus K_{hyd} obtained from the hydrostatic oscillations to validate the assumption of isotropy and to check the consistency of the results.

2.3. Attenuation — Q^{-1} Measurements

The factor Q^{-1} measures the elastic energy dissipation within the sample. When this dissipation occurs, the rheology of the medium is similar to a viscoelastic material [*O'Connell and Budiansky*, 1977]. The stress-strain curve presents an elliptic shape that clearly highlights the nonelastic behavior (e.g., Figures 2b and 2d). This results from the phase shift between the stress and the strain (equation (2)). During a dynamic oscillation of frequency f, the complex stress can be expressed as $\bar{\sigma} = \sigma e^{i(2\pi ft+\phi_\sigma)}$ and the resulting complex strain $\bar{\varepsilon} = \varepsilon e^{i(2\pi ft+\phi_\varepsilon)}$, where ϕ_σ and ϕ_ε are the phases of $\bar{\sigma}$ and $\bar{\varepsilon}$. For each elastic modulus, the calculation of the Q^{-1} factor is based on the causality principle, where the complex modulus $\bar{M}$ relates the stress $\bar{\sigma}$ to its resulting strain $\bar{\varepsilon}$:

$$\bar{\sigma} = \bar{M}\bar{\varepsilon}. \tag{6}$$

21699356, 2017, 4, Downloaded from https://agupubs.onlinelibrary.wiley.com/doi/10.1002/2016JB013816 by Cochrane France, Wiley Online Library on [08/02/2023]. See the Terms and Conditions (https://onlinelibrary.wiley.com/terms-and-conditions) on Wiley Online Library for rules of use; OA articles are governed by the applicable Creative Commons License

The factor Q_M^{-1} of the modulus $\bar{M}$ is then defined as follows [*O'Connell and Budiansky*, 1978]:

$$Q_M^{-1} = \frac{\mathrm{Im}(\bar{M})}{\mathrm{Re}(\bar{M})} = \frac{\mathrm{Im}\left(\bar{\sigma}/\bar{\varepsilon}\right)}{\mathrm{Im}\left(\bar{\sigma}/\bar{\varepsilon}\right)} = \tan\left(\phi_\sigma - \phi_\varepsilon\right), \tag{7}$$

In the case of the bulk modulus measured from hydrostatic oscillations, $Q_{K_{\mathrm{hyd}}}^{-1}$ is deduced from the phase shift between the hydrostatic stress $-\Delta P_c$, with the convention $\Delta P_c = -\sigma_{ii}/3$, and the volumetric strain $\varepsilon_{\mathrm{vol}}$. With the combination of equations (3) and (7), we obtain the following:

$$Q_{K_{\mathrm{hyd}}}^{-1} = \tan\left(\phi_{-\Delta P_c} - \phi_{\varepsilon_{\mathrm{vol}}}\right). \tag{8}$$

The Young's modulus and Poisson's ratio factors Q_E^{-1} and Q_ν^{-1} are deduced from equations (4) and (7):

$$Q_E^{-1} = \tan\left(\phi_{\sigma_{\mathrm{ax}}} - \phi_{\varepsilon_{\mathrm{ax}}}\right) \quad \text{and} \quad Q_\nu^{-1} = \tan\left(\phi_{\varepsilon_{\mathrm{ax}}} - \phi_{\varepsilon_{\mathrm{rad}}}\right). \tag{9}$$

To derive Q^{-1} for K_{ax} and G_{ax}, with the assumptions of isotropy and small strains, we combine equations (4) and (5) as follows:

$$K_{\mathrm{ax}} = \frac{1}{3}.\frac{\sigma_{\mathrm{ax}}}{\varepsilon_{\mathrm{ax}} + 2\varepsilon_{\mathrm{rad}}} \quad \text{and} \quad G_{\mathrm{ax}} = \frac{1}{2}.\frac{\sigma_{\mathrm{ax}}}{\varepsilon_{\mathrm{ax}} - \varepsilon_{\mathrm{rad}}}. \tag{10}$$

For both K_{ax} and G_{ax} the stress is σ_{ax} and the resulting strains are, respectively, $\varepsilon_{\mathrm{ax}} + 2\varepsilon_{\mathrm{rad}}$ and $\varepsilon_{\mathrm{ax}} - \varepsilon_{\mathrm{rad}}$. After combining equations (7) and (10), the related attenuations are as follows:

$$Q_{K_{\mathrm{ax}}}^{-1} = \tan\left(\phi_{\sigma_{\mathrm{ax}}} - \phi_{\varepsilon_{\mathrm{ax}}+2\varepsilon_{\mathrm{rad}}}\right) \quad \text{and} \quad Q_{G_{\mathrm{ax}}}^{-1} = \tan\left(\phi_{\sigma_{\mathrm{ax}}} - \phi_{\varepsilon_{\mathrm{ax}}-\varepsilon_{\mathrm{rad}}}\right) \tag{11}$$

Three different methods can be used to calculate the Q^{-1} factors [e.g., *Tisato and Madonna*, 2012]. The first method consists of fitting two sine functions $y = A\sin(2\pi f + \phi)$ through the stress and strain signals and extract ϕ from each signal to calculate the phase shift $\phi_\sigma - \phi_\varepsilon$. The second method consists in extracting the phases from a Fourier analysis of the signals. For this purpose a fast Fourier transform (FFT) algorithm is applied on the stress and strain signals. And finally, the last method is based on the definition of Q^{-1} factor that relates Q^{-1} to the dissipated elastic energy (ΔE) during a stress-strain cycle and to the average elastic energy stored (E_m) as follows [*O'Connell and Budiansky*, 1978]:

$$Q^{-1} = \frac{\Delta E}{4\pi E_m}. \tag{12}$$

When viscous dissipation occurs in the fluid, the stress-strain curve presents an elliptic shape, similarly to viscoelastic materials (e.g., Figures 2b and 2d). The dissipated energy ΔE is equal to the surface of this ellipse, and E_m is equal to the average surface under the stress-strain curve. The surfaces that represent ΔE and E_m can be calculated from the stress versus strain curve by numerical integration [*Tisato and Madonna*, 2012]:

$$\Delta E = \sum_{n=1}^{N-1} \frac{\left(\sigma_{n+1} + \sigma_n\right)\left(\varepsilon_{n+1} - \varepsilon_n\right)}{2N_c} \quad \text{and} \quad E_m = \sum_{n=1}^{N} \frac{\sigma_n \varepsilon_n}{2N}, \tag{13}$$

where σ_n and ε_n are all the data points of, respectively, $\bar{\sigma}$ and $\bar{\varepsilon}$ signals during one recording, N is the total number of sampled data and $N_c = f.t_{\mathrm{tot}}$ is the number of cycles, f being the frequency of the oscillation, and t_{tot} the total time of the sequence. For simplicity, the three methods presented above are, respectively, denominated as "Sines," "FFT," and "Ellipse" methods in the following text. The experimental measurements presented later in the results section were calculated from the Ellipse method, and comparison between the three methods will be provided for the axial oscillations.

The relation between the dispersion and the attenuation of the complex modulus, $\bar{M}$, arises from the causality principle between the stress and strain that is expressed through the Kramers-Kronig equations [*Mikhaltsevitch et al.*, 2016b]. If $\bar{M} = M_R + iM_I$, with i the imaginary unit, M_R the real part, and M_I the imaginary part of $\bar{M}$, an approximation of the Kramers-Kronig equations was found by *O'Donnell et al.* [1981]:

$$M_I(\omega) = \frac{\pi}{2}\omega\frac{dM_R(\omega)}{d\omega}, \tag{14}$$

21699356, 2017, 4, Downloaded from https://agupubs.onlinelibrary.wiley.com/doi/10.1002/2016JB013816 by Cochrane France, Wiley Online Library on [08/02/2023]. See the Terms and Conditions (https://onlinelibrary.wiley.com/terms-and-conditions) on Wiley Online Library for rules of use; OA articles are governed by the applicable Creative Commons License

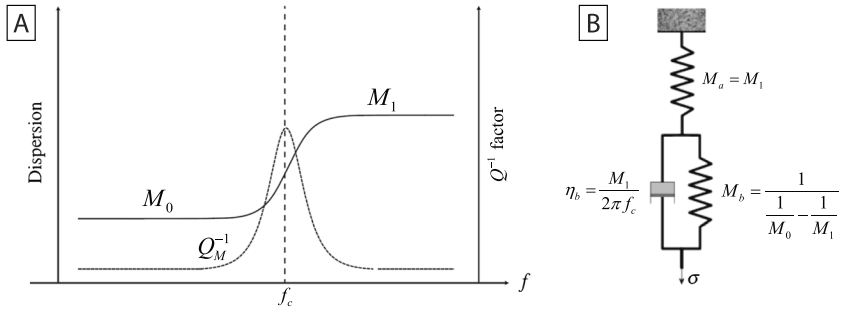

Figure 3. Zener's viscoelastic model used to calculate the attenuation from the dispersion. (a) Model applied to the dispersion of the modulus M of relaxed value M_0 and unrelaxed value M_1. (b) Spring-damper representation of Zener's model, with the relationships between the springs elastic moduli (M_a and M_b) and dispersion's relaxed and unrelaxed values (M_0 and M_1). The viscosity (η_b) of the damper is a function of M_1 and the cutoff frequency f_c: $\eta_b = M_1/2\pi f_c$.

where $\omega = 2\pi f$. The major drawback of applying equation (14) to experimental data is that an accurate calculation of the derivative $dM_R/d\omega$ by finite difference requires a good resolution in ω.

Because our experimental measurements did not necessarily have a proper resolution in ω, the consistency between the measured dispersion and attenuation was verified instead with a Zener viscoelastic model [*Pimienta et al.*, 2015a]. The equivalent spring-damper model is represented in Figure 3b, and its transfer function $\bar{M}$ can be expressed with the viscoelastic parameters of the system:

$$\bar{M} = \frac{1 + i\omega\tau}{\left(\frac{1}{M_a} + \frac{1}{M_b}\right) + \frac{i\omega\tau}{M_a}}, \tag{15}$$

where M_a and M_b are the moduli of the two springs and $\tau = \eta_b/M_b$ where η_b is the viscosity of the dashpot element (Figure 3b). This model follows the assumption that only one viscous dissipation mechanism is involved. With the approximation $M_a \ll M_b$, equations (7) and (15) give the following:

$$Q_M^{-1} \simeq \frac{\omega\tau}{1 + \omega^2\tau^2}\frac{M_a}{M_b}. \tag{16}$$

If we consider a dispersive transition where the sample's modulus ($\bar{M}$) varies from M_0 to M_1 around the cutoff frequency f_c (Figure 3a), the elastic parameters of the Zener model become $M_a = M_1$ and ${M_b}^{-1} = {M_0}^{-1} - {M_1}^{-1}$, and the viscosity of the dashpot becomes $\eta_b = M_1/2\pi f_c$ (Figure 3b). Therefore, only three parameters are required to calculate the Q^{-1} factor from Zener's model: the moduli M_0 and M_1 and the cutoff frequency f_c. It is to note here that if the dispersion is related to the global flow, M_0 and M_1 would be the drained and undrained (isobaric) moduli. If the dispersion is related to squirt flow, M_0 and M_1 would be the undrained (isobaric) and unrelaxed (isolated) moduli.

2.4. Ultrasonic Measurements

In addition to the stress-strain oscillations, the apparatus enables the measurement of ultrasonic (~ 1 MHz) moduli from *P* and *S* wave transducers, glued in the end platens at both ends on the sample (Figure 1a). *P* and *S* wave velocities V_P and V_S are inferred from the traveltime (Δt) of the ultrasonic waves through the sample's length (L = 80 mm), after correction of the traveltime through the end platens. The arrival times of the *P* and *S* waves are handpicked with a maximum error of ±0.1μs. The velocity (V) is then calculated by $V = L/\Delta t$. With a maximum error on L of ±0.01 mm, the relative uncertainty on the velocities is about $\Delta V/V$ = 0.5%. The high-frequency moduli K_{HF} and G_{HF} are obtained by the well-known formulas:

$$K_{HF} = \rho\left({V_P}^2 - \frac{4}{3}{V_S}^2\right) \quad \text{and} \quad G_{HF} = \rho{V_S}^2, \tag{17}$$

where ρ_{sample} is the density of the medium, calculated from the density of the dry sample ρ_{dry} = 2160 kg m^{-3}, the density of the saturating fluid ρ_{fluid}, and the porosity ϕ by $\rho_{sample} = \rho_{dry} + \phi.\rho_{fluid}$. The densities of glycerin and water are, respectively, ρ_{gly} = 1250 kg/m^3 and ρ_{water} = 1000 kg/m^3 [*Bosart and Snoddy*, 1927]. With a relative uncertainty on ρ estimated around 1%, the relative uncertainty of the product ρV^2 is about 2%. From this we can deduce the relative uncertainties $\Delta K_{HF}/K_{HF} \simeq 4\%$ and $\Delta G_{HF}/G_{HF} \simeq 2$ for, respectively, the ultrasonic

21699356, 2017, 4, Downloaded from https://agupubs.onlinelibrary.wiley.com/doi/10.1002/2016JB013816 by Cochrane France, Wiley Online Library on [08/02/2023]. See the Terms and Conditions (https://onlinelibrary.wiley.com/terms-and-conditions) on Wiley Online Library for rules of use; OA articles are governed by the applicable Creative Commons License

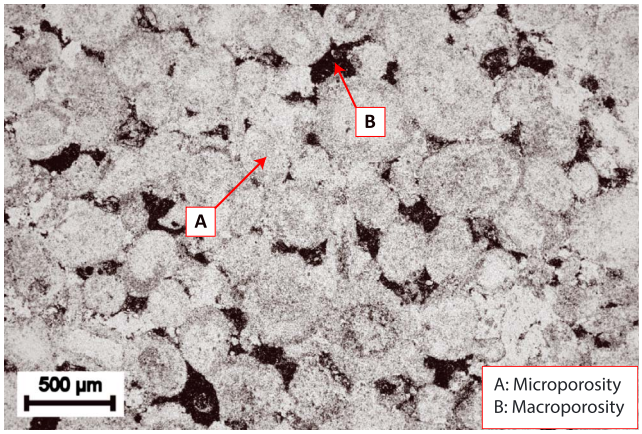

Figure 4. SEM photomicrograph of the Lavoux sample. The sample is a pure calcite grainstone composed of microporous oolites (marker A), surrounded by macropores (marker B). The average size of the oolites is around 300µm.

bulk and shear modulus. Before measuring the traveltimes of the elastic waves in the sample, an aluminum standard (2007A/AU4G) of 80 mm length was measured to calibrate the traveltimes in the top and bottom end platens.

3. Sample Description

The studied sample is a Lavoux limestone that was quarried in Paris Basin and was extensively studied in the literature [e.g., *Fabre and Gustkiewicz*, 1997; *Rasolofosaon and Zinszner*, 2002; *Youssef et al.*, 2008; *Bemer and Lombard*, 2010; *Vincent et al.*, 2011; *Zinsmeister*, 2013]. It is from Dogger age and is considered as an analogue to the White Oolitic Formation of Paris Basin [*Bemer and Lombard*, 2010]. It is a pure calcite oolitic grainstone with intergranular macroporosity and intragranular microporosity (Figure 4). Mercury porosimetry measurements from *Zinsmeister* [2013] or *Vincent et al.* [2011] confirm the presence of a connected bimodal porosity distribution with pore entry diameters around 0.6 µm and 20 µm, which corresponds, respectively, to the intra-oolite micropores and the interoolite macropores. Moreover, the NMR unimodal distribution results from *Vincent et al.* [2011] were interpreted as indicating a good connectivity between the intragranular-micropore network and the intergranular-macropore network.

The porosity was measured around 23% from the triple-weight method, where the sample's mass is measured under three different conditions: dry, fluid saturated, and suspended in the saturant. Image analysis of the SEM photomicrograph enables to evaluate the proportion of macroporosity in the total porosity. A threshold was applied on the gray scale of the photomicrograph to turn it into a binary image showing solely the macropores (Figure 5). The macropores' proportion in the binary image, combined with the previous

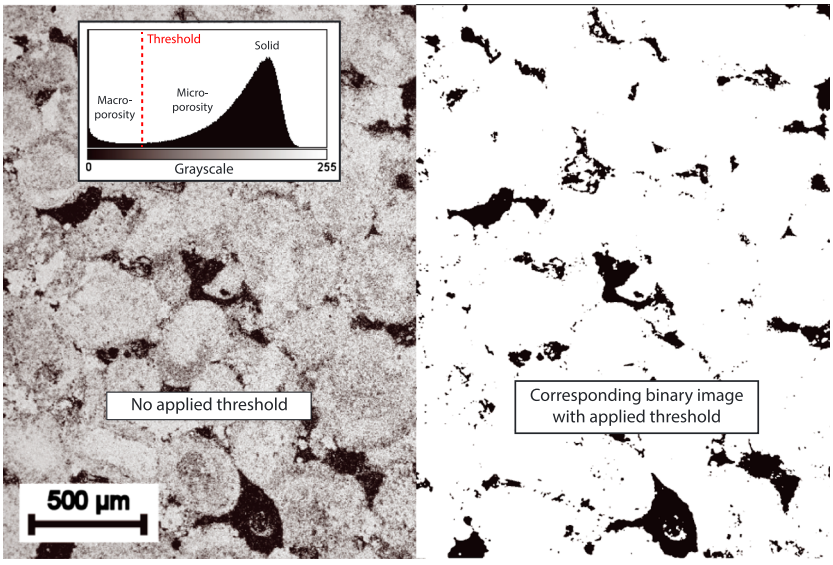

Figure 5. Determination of the proportion macroporosity/microporosity in the sample from the gray scale analysis of the SEM photomicrograph. A threshold is applied on the initial photomicrograph (left), to create a binary image representing solely the macropores (right). The porosity of the macropores is calculated from the number of black pixels over the total number of pixels of the image, evaluated at 10.35%. With a total porosity of 23% measured experimentally, the proportion of macroporosity over microporsity is therefore around 45/55.

21699356, 2017, 4, Downloaded from https://agupubs.onlinelibrary.wiley.com/doi/10.1002/2016JB013816 by Cochrane France, Wiley Online Library on [08/02/2023]. See the Terms and Conditions (https://onlinelibrary.wiley.com/terms-and-conditions) on Wiley Online Library for rules of use; OA articles are governed by the applicable Creative Commons License

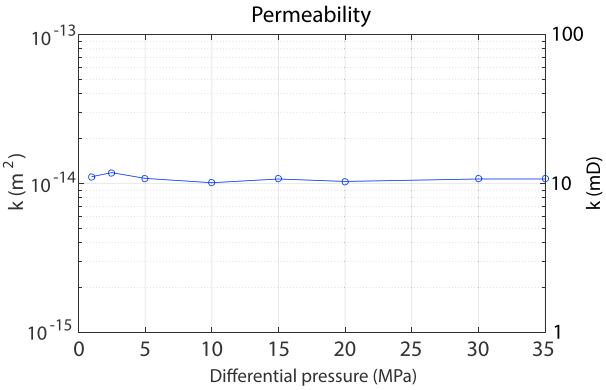

Figure 6. Intrinsic permeability of the Lavoux sample as a function of differential pressure. The measurements were obtained by Darcy's law under water-saturated conditions. The results show no dependence to the effective pressure.

experimental porosity, gives a contribution to the total porosity of 45% and 55% for the macroporosity and the microporosity, respectively. The permeability was measured to be around 10 mD, under water-saturated conditions, and shows no dependence to differential pressure (Figure 6).

4. Results

4.1. Pressure Dependence of the Sample's Elastic Properties

Ultrasonic measurements and the axial oscillations have been performed at differential pressures from 2.5 MPa to 20 MPa, to check the pressure dependence of the elastic moduli. The traveltimes measured for the Lavoux limestone are reported in Table 1, along with the deduced *P* wave and *S* wave velocities and high-frequency moduli K_{HF} and G_{HF} (equation (17)). K_{HF} and G_{HF} for dry-, water-, and glycerin-saturated conditions as a function of differential pressure are represented in Figure 7. No variation in pressure is to be noted. K_{HF} is constant at about 14.5 GPa, 21.5 GPa, and 25.5 GPa, respectively, for the dry-, water-, and glycerin-saturated conditions. We can see that the fluid nature strongly affects the high-frequency bulk moduli. On the other hand, G_{HF} remains constant at 9.5 GPa, with no sensitivity to the fluid nature.

For the axial oscillations at different pressures, the Young's modulus (E) and Poisson's ratio (ν) results measured at 5×10^{-2} Hz, 10^{-1} Hz, and 5 Hz are presented in Figure 8. Again, no dependence to differential pressure is observed, either for Young's modulus (Figure 8a) or Poisson's ratio (Figure 8b). Under dry conditions, no dependence to f is observed. Under glycerin-saturated conditions, nearly no dependence to f is observed on E (Figure 8a), but a large one is observed on ν (Figure 8b).

We can conclude that, similarly to the permeability, the elastic properties of the Lavoux limestone seem to not depend on the differential pressure. Therefore, in the following, all the results will be presented solely for a differential pressure of 2.5 MPa and can be considered as independent of differential pressure.

4.2. Axial Stress Oscillations Results at $P_{diff} = 2.5$ MPa

The dispersion and attenuation results from the axial and the hydrostatic oscillations under dry-, water-, and glycerin-saturated conditions are presented in Figures 9–11. The results are represented as a function of an

Table 1. Ultrasonic Measurements (1 MHz) on the Lavoux Limestone Under Dry-, Water-, and Glycerin-Saturated Conditions[a]

Saturating Fluid	P_{diff} (MPa)	t_P (μs)	t_S (μs)	V_P (m s^{-1})	V_S (m s^{-1})	K_{HF} (GPa)	G_{HF} (GPa)
	2.5	23.0	38.5	3520	2103	14.0	9.6
Dry	5	22.4	38.0	3614	2131	15.4	9.8
$\rho_{sample} = 2160$ kg m^{-3}	10	23.0	38.0	3520	2131	13.7	9.8
	15	22.4	38.0	3614	2131	15.1	9.8
	20	22.5	38.0	3598	2131	14.9	9.8
Water	2.5	21.4	40.8	3783	1984	21.7	9.4
$\rho_{sample} = 2391$ kg m^{-3}	10	21.5	40.6	3766	1994	21.2	9.5
	2.5	20.6	42.3	3930	1914	25.9	9.0
Glycerin	5	20.4	42.2	3969	1918	26.5	9.0
$\rho_{sample} = 2448$ kg m^{-3}	10	20.8	42.0	3892	1928	25.0	9.1
	15	20.7	41.6	3911	1946	25.1	9.3
	20	20.6	41.4	3930	1956	25.3	9.4

[a]The traveltimes t_P and t_S were corrected from the traveltimes in the end platens. The length of the sample is 80 mm. K_{HF} and G_{HF} are deduced from equation (17).

21699356, 2017, 4, Downloaded from https://agupubs.onlinelibrary.wiley.com/doi/10.1002/2016JB013816 by Cochrane France, Wiley Online Library on [08/02/2023]. See the Terms and Conditions (https://onlinelibrary.wiley.com/terms-and-conditions) on Wiley Online Library for rules of use; OA articles are governed by the applicable Creative Commons License

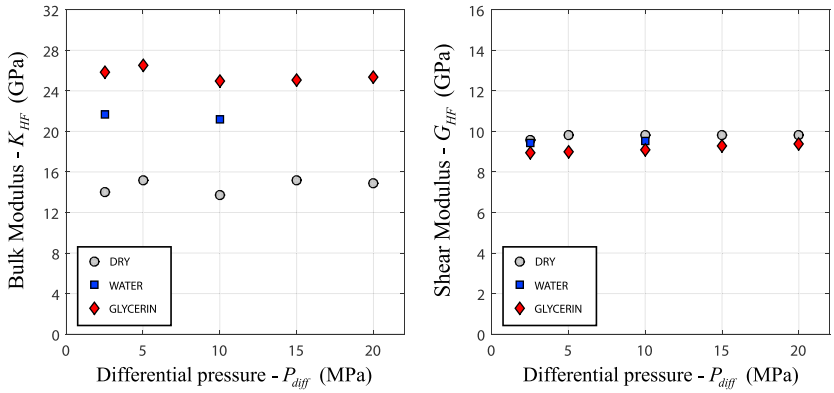

Figure 7. Ultrasonic results (1 MHz) at different differential pressures ($P_{diff} = P_c - p_f$) for (left) the bulk modulus (K_{HF}) and (right) the shear modulus (G_{HF}), for dry-, water-, and glycerin-saturated conditions.

apparent frequency $f^* = f.(\eta_{fluid}/\eta_{water})$ to take into account the effect of the fluid's viscosity, with water as the reference fluid ($\eta_{water} = 10^{-3}$ Pa s). For dry conditions, the viscosity of air is considered at about $\eta_{air} = 10^{-5}$ Pa s. The Q^{-1} factor results are calculated from the Ellipse method and are systematically compared to Zener's viscoelastic model. The measurements are done with the valves of the drainage circuit open (Figure 1a), i.e., in drained boundary conditions, with a pore pressure of $p_f = 2$ MPa.

The Young's modulus and Poisson's ratio dispersion and attenuation results from the axial oscillations at $P_{diff} = 2.5$ MPa are presented in Figure 9. The Young's modulus (E) is constant around 22.5 GPa between 10^{-3} Hz and 10^2 Hz, with a good agreement between the dry, water, and glycerin saturations (Figure 9a). Then, E increases slightly between 10^2 Hz and 10^3 Hz from 22.5 GPa to 24 GPa (Figure 9a). The factor Q_E^{-1} results are consistent with the dispersion data: no attenuation under 10^2 Hz, a small peak around $Q_E^{-1} = 0.025$ at 3×10^2 Hz, and no more attenuation beyond 10^3 Hz (Figure 9b). Moreover, the results are in good agreement with Zener's model, using the parameters $M_0 = 22.5$ GPa, $M_1 = 24$ GPa, and $f_c = 220$ Hz (Figure 3).

Similarly to E, the Poisson's ratio (ν) below 10^2 Hz shows no dispersion, but a slight disagreement subsists between the dry- ($\nu = 0.25$) and the water- and glycerin-saturated results ($\nu = 0.275$) (Figure 9c). Then ν increases from 0.275 to 0.35 between 5×10^1 Hz and 10^3 Hz (Figure 9c), in correlation with a Q_ν^{-1} peak of 0.08 at around 3×10^2 Hz (Figure 9d). For this case, Zener's model seems to overpredict the attenuation. The Zener peak is around 0.13 at 3×10^2 Hz, with the parameters $M_0 = 0.275$ and $M_1 = 0.35$. (Figure 9d).

Assuming isotropic conditions, the dispersion and attenuation results of the bulk modulus and the shear modulus, deduced from E and ν, are presented in Figure 10. The bulk modulus deduced from the axial oscillations (K_{ax}) shows a large dispersion from 16 GPa to 26 GPa between $f^* = 5 \times 10^1$ Hz and $f^* = 10^3$ Hz, visible under glycerin-saturated conditions (Figure 10a). The corresponding attenuation peak reaches $Q_{K_{ax}}^{-1} = 0.225$ around $f^* = 3 \times 10^2$ Hz with a good fit with Zener's model with the parameters $M_0 = 16$ GPa and $M_1 = 26$ GPa. The shear

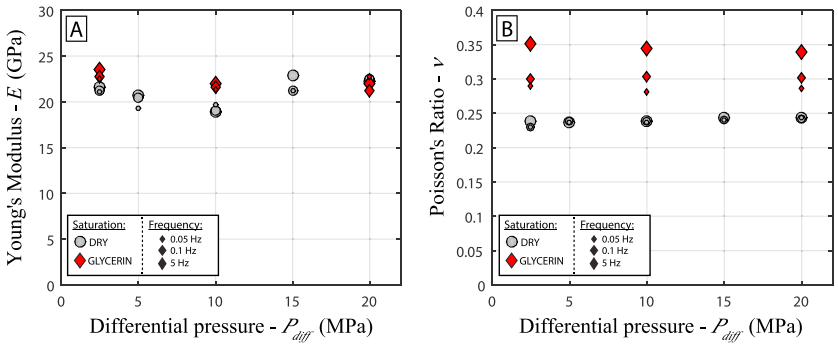

Figure 8. Axial oscillations results at different differential pressures ($P_{diff} = P_c - p_f$) for (a) Young's modulus (E) and (b) Poisson's ratio (ν). The results for dry- and glycerin-saturated conditions are presented, for 0.05 Hz, 0.1 Hz, and 5 Hz.

21699356, 2017, 4, Downloaded from https://agupubs.onlinelibrary.wiley.com/doi/10.1002/2016JB013816 by Cochrane France, Wiley Online Library on [08/02/2023]. See the Terms and Conditions (https://onlinelibrary.wiley.com/terms-and-conditions) on Wiley Online Library for rules of use; OA articles are governed by the applicable Creative Commons License

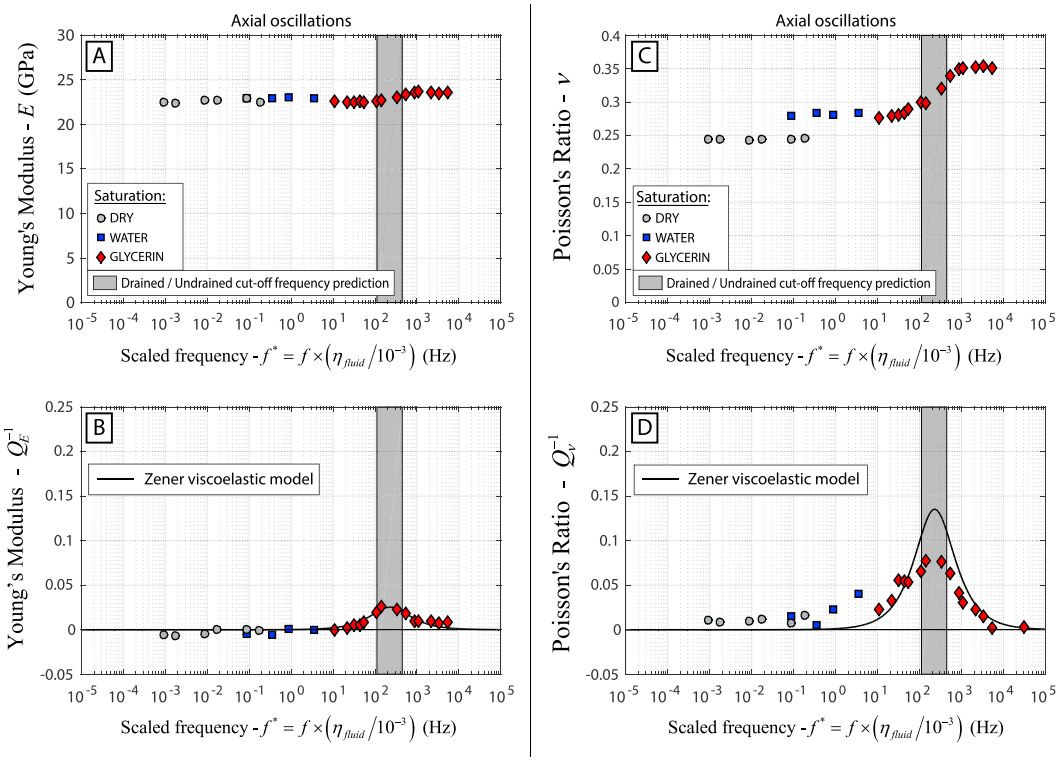

Figure 9. (a) Young's modulus E, (b) Q_E^{-1}, (c) Poisson's ratio ν, and (d) Q_ν^{-1} resulting from the axial oscillations at $P_{diff} = 2.5$ MPa, under dry-, water-, and glycerin-saturated conditions. The frequency is scaled with the viscosity of the saturating fluid η_{fluid}. The factors Q_E^{-1} and Q_ν^{-1} are compared to Zener's model. The range for the drained/undrained cutoff frequency f_1^* is represented by the gray area.

modulus G_{ax} shows no dispersion at all, with a constant value around $G_{ax} = 9$ GPa (Figure 10c). Consistently, the related attenuation $Q_{G_{ax}}^{-1}$ is nil throughout the whole frequency range (Figure 10d).

4.3. Hydrostatic Oscillations Results at $P_{diff} = 2.5$ MPa

The results of the purely hydrostatic oscillations at $P_{diff} = 2.5$ MPa are presented in Figure 11. The measured bulk modulus K_{hyd} shows a dispersion from 16 GPa to 25 GPa between $f^* = 2\times10^1$ Hz and $f^* = 4\times10^2$Hz, visible under glycerin-saturated conditions (Figure 11a). The related factor $Q_{K_{hyd}}^{-1}$ has a peak at about $Q_{K_{hyd}}^{-1} = 0.22$ around $f^* = 2 \times 10^2$ Hz and is nil elsewhere (Figure 11b). The attenuation seems to compare well with Zener's model with the parameters used previously for K_{ax} ($M_0 = 16$ GPa, $M_1 = 26$ GPa) (Figure 11b).

4.4. Uncertainty Analysis

For the hydrostatic oscillations, the uncertainty on the bulk modulus measurements (δK) depends on the confining pressure uncertainty (δP) and the uncertainty of the strain measurements ($\delta\varepsilon$). From equation (3), the relative uncertainty on K is given by:

$$\frac{\delta K_{hyd}}{K_{hyd}} = \frac{\delta P}{P} + \frac{\delta\varepsilon}{\varepsilon}. \tag{18}$$

The pressure sensor of the confining cell is capable to measure pressure with a resolution of $\delta P = 0.001$ MPa. The amplitude of the confining pressure oscillations being around 0.2 MPa, the relative uncertainty on pressure becomes $\delta P/P = 0.005$, which can be considered negligible. Therefore, the uncertainty on the bulk modulus highly depends on the quality of the strain measurement. The higher the number of strain gauges, the lower this uncertainty becomes. A total of $n = 8$ strain gauges was used (four axial and four radial). When proceeding with the oscillations, the amplitude of the strain gauges may vary slightly from one another. These variations could be related to the quality of the contact between the strain gauge and the sample or to small heterogeneities in the sample despite being considered perfectly homogeneous. Although the orientation of the strain gauges relatively to the vertical and horizontal axis can be determinant for axial oscillations, it is

21699356, 2017, 4, Downloaded from https://agupubs.onlinelibrary.wiley.com/doi/10.1002/2016JB013816 by Cochrane France, Wiley Online Library on [08/02/2023]. See the Terms and Conditions (https://onlinelibrary.wiley.com/terms-and-conditions) on Wiley Online Library for rules of use; OA articles are governed by the applicable Creative Commons License

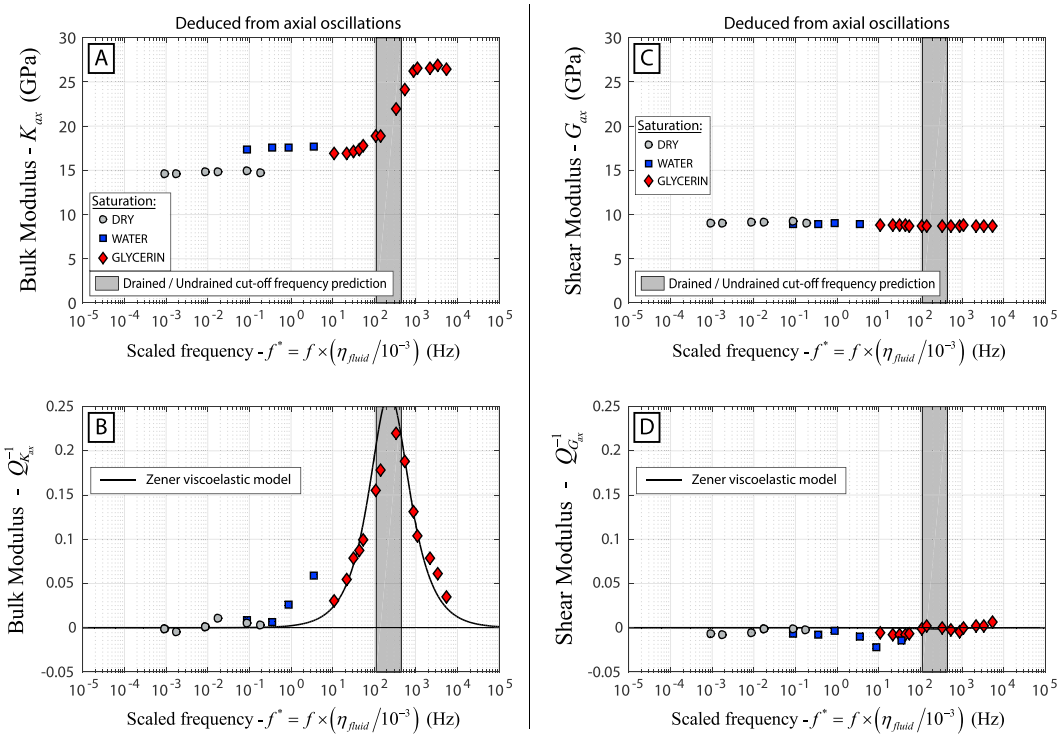

Figure 10. (a) Bulk modulus K_{ax}, (b) $Q^{-1}_{K_{ax}}$, (c) shear modulus G_{ax}, and (d) $Q^{-1}_{G_{ax}}$ deduced from the results of the axial oscillations (Figure 9). K_{ax} and G_{ax} are deduced from E and ν (equation (5)) under the assumption of an isotropic medium. $Q^{-1}_{K_{ax}}$ and $Q^{-1}_{G_{ax}}$, deduced from equations (10) and (11), are compared to Zener's model. The frequency is scaled with the viscosity of the saturating fluid η_{fluid}. The range for the drained/undrained cutoff frequency f_1^* is represented by the gray area.

irrelevant for hydrostatic oscillations on an isotropic medium. For the hydrostatic oscillations at $f = 0.004$ Hz and $P_{diff} = 2.5$ MPa, the average of the eight measured strain was $\varepsilon = 2.22$ μm/m, with a standard deviation of $std = 0.266$ μm/m. The error on the average strain ($\delta\varepsilon$) can be calculated from $\delta\varepsilon = std/\sqrt{n} = 0.094$ μm/m. From equation (18), we deduce the relative uncertainty on K_{hyd} for the hydrostatic oscillations: $\delta K_{hyd}/K_{hyd} = 4.2\%$. This corresponds to an error of about ± 0.3 GPa for K_{hyd}.

The similar approach can be done to calculate the uncertainties for the axial oscillations results. From equation (4), we can deduce the following:

$$\frac{\delta E}{E} = \frac{\delta\varepsilon_{alu}}{\varepsilon_{alu}} + \frac{\delta\varepsilon_{ax}}{\varepsilon_{ax}} \quad \text{and} \quad \frac{\delta\nu}{\nu} = \frac{\delta\varepsilon_{rad}}{\varepsilon_{rad}} + \frac{\delta\varepsilon_{ax}}{\varepsilon_{ax}}. \tag{19}$$

With two strain gauges measuring ε_{alu}, four measuring ε_{ax}, and four measuring ε_{rad}, the relative uncertainties on E and ν were found to be $\delta E/E = 12\%$ and $\delta\nu/\nu = 8\%$. These uncertainties correspond to errors of ± 1.3 GPa for E and ± 0.01 for ν. We can then use equation (5) to propagate the error to K_{ax} and G_{ax}. This gives an error of ± 1.5 GPa for K_{ax} and ± 0.6 GPa for G_{ax}.

4.5. Comparison of the Three Methods Used to Infer Q^{-1}

Q^{-1} factors of all the elastic properties deduced from the axial oscillations at $P_{diff} = 2.5$ MPa under glycerin-saturated conditions were also calculated using the Sines and the FFT method. Those are compared to the previously presented results from the Ellipse method (Figure 12). For E, K_{ax}, and G_{ax} (respectively Figures 12a, 12c, and 12d) the three methods compare well over the experimental frequency range $f \in [2 \times 10^{-2}\,;\,5]$ Hz. In case of ν (Figure 12b), the FFT and Ellipse methods are consistent with each other but not with the Sines method. The results obtained with the Sines method for ν are unstable and give erratic results with data points off the chart (Figure 12b). The Sines method shows also some slight inconsistencies with the other methods at 10^{-2} Hz for E and K_{ax} (Figures 12a and 12c). We can therefore conclude that only the Ellipse and FFT methods are reliable to calculate Q^{-1} in our case.

21699356, 2017, 4, Downloaded from https://agupubs.onlinelibrary.wiley.com/doi/10.1002/2016JB013816 by Cochrane France, Wiley Online Library on [08/02/2023]. See the Terms and Conditions (https://onlinelibrary.wiley.com/terms-and-conditions) on Wiley Online Library for rules of use; OA articles are governed by the applicable Creative Commons License

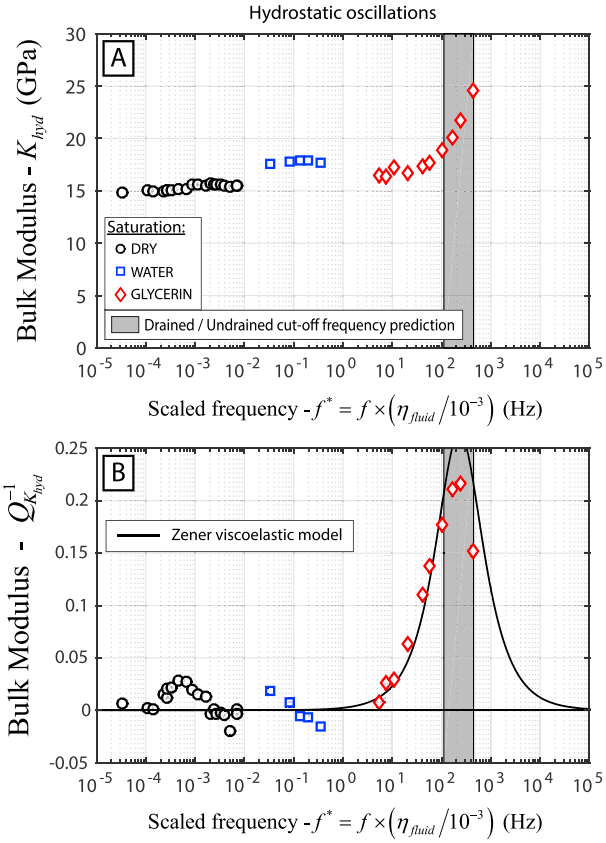

Figure 11. (a) Bulk modulus K_{hyd} and (b) $Q^{-1}_{K_{hyd}}$ resulting from the hydrostatic oscillations at $P_{diff} = 2.5$MPa, under dry-, water-, and glycerin-saturated conditions. The frequency is scaled with the viscosity of the saturating fluid η_{fluid}. The factor $Q^{-1}_{K_{hyd}}$ is compared with Zener's model. The range for the drained/undrained cutoff frequency f_1^* is represented by the gray area.

5. Discussion

5.1. The Drained and Undrained Regimes

With respect to the cutoff frequencies (equation (1)), and especially the drained/undrained cutoff frequency, a viscosity contrast for the fluid results in a shift in frequency of the transition. The results presented with the three different saturating fluids show a good continuity in scaled frequency (Figure 13). A slight discrepancy exists between the dry- and water-saturated conditions, the dry bulk modulus being about 2.5 GPa lower than the water-saturated bulk modulus (Figure 13a). This discrepancy is seen in both the hydrostatic and axial oscillations and seems larger than the uncertainties of the measurements (Figure 13a). It is possible that the sample was not fully dry during the measurements, with the presence of moisture that would induce a weakening effect. Although this effect is known to be important in sandstones and rather negligible in limestones [*Clark et al.*, 1980; *Pimienta et al.*, 2014], measurements on a Leuders limestone from *Clark et al.* [1980] still show an increase of about 5 GPa for K and 0.04 for ν when going from a relative humidity of 35% (ambient room) to a vacuum state.

The drained/undrained cutoff frequency (f_1) was experimentally measured around 2×10^{-1} Hz in glycerin-saturated conditions, which is a frequency that is equivalent to 2×10^{2} Hz in water-saturated conditions. Therefore, when studying dispersion and attenuation phenomenon related to diffusion processes at different scales, the experimental frequencies can be scaled by the dynamic viscosity of the fluid η [*Pimienta et al.*, 2015a, 2015b, 2016a; *Spencer and Shine*, 2016]. This has the major advantage to increase the apparent frequency range reachable by the experimental setup up, in our case for the axial oscillations from $10^{-2} - 10^{1}$ Hz to $10^{-4} - 10^{4}$ Hz, and therefore characterize the dispersion of the sample over a much larger frequency band.

21699356, 2017, 4, Downloaded from https://agupubs.onlinelibrary.wiley.com/doi/10.1002/2016JB013816 by Cochrane France, Wiley Online Library on [08/02/2023]. See the Terms and Conditions (https://onlinelibrary.wiley.com/terms-and-conditions) on Wiley Online Library for rules of use; OA articles are governed by the applicable Creative Commons License

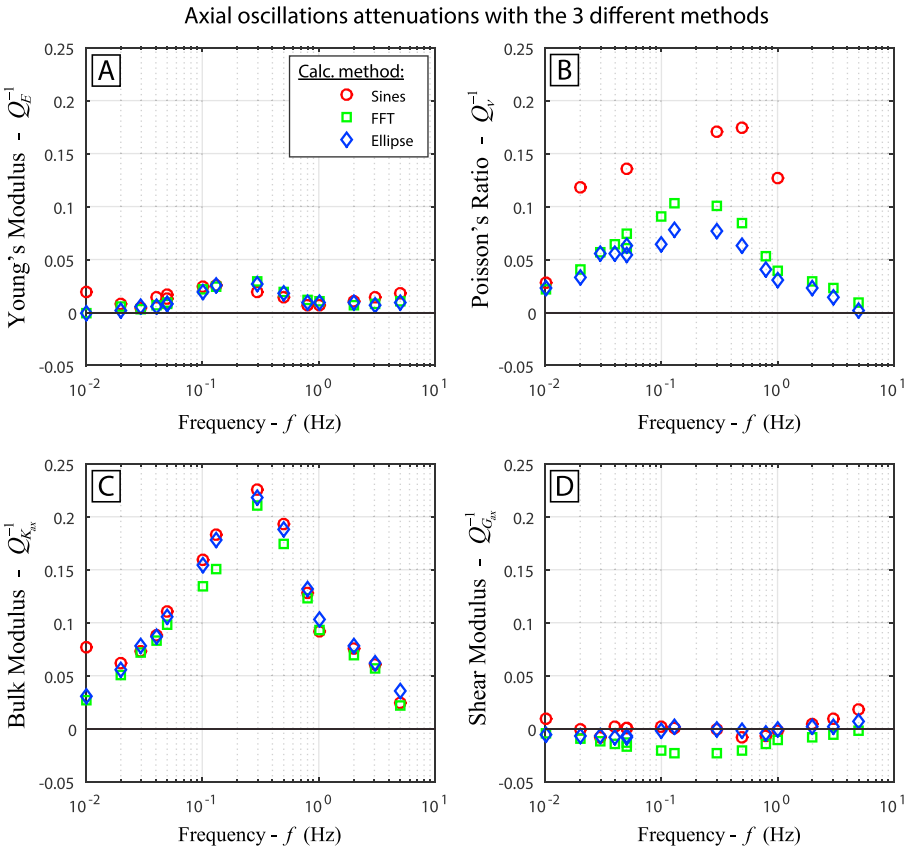

Figure 12. Comparison of the three methods used to calculate Q^{-1}: Sines, FFT, and Ellipse methods. Example for the axial oscillations at P_{diff} = 2.5 MPa under glycerin-saturated conditions, for (a) Young's modulus, (b) Poisson's ratio, (c) bulk modulus, and (d) the shear modulus.

5.1.1. Elastic Moduli

The common elastic modulus we can extract from the hydrostatic and axial oscillations is the bulk modulus, respectively, K_{hyd} and K_{ax} (deduced from E and ν). The comparison between the dispersion and Q^{-1} of both moduli at P_{diff} =2.5 MPa is presented in Figure 13. The hydrostatic and axial results compare well over their overlapping frequencies, both for the dispersion (Figure 13a) and for Q^{-1} (Figure 13b). This tends to validate our hypothesis of an isotropic medium and shows a good consistency between both stress-strain methods for the drained and undrained regimes.

Using the measured permeability value (i.e., $\kappa = 10^{-14}$ m^2) and the dry bulk modulus (i.e., K_d=15 GPa) and assuming a diffusion length L in the sample between 40 mm and 80 mm, the expected cutoff frequency f_1^* for the drained/undrained transition (equation (1)) is between 10^2 Hz and 4×10^2 Hz. All the previous dispersions and Q^{-1} results are in agreement with this frequency transition (Figures 9–11, and 13). The maximum Q^{-1} peaks for E, ν, K_{ax}, and K_{hyd}, and the dispersion slopes of the elastic moduli are systematically in the expected range of f_1^* (Figures 9–11, and 13).

The undrained elastic properties of a rock are generally deduced from the drained (or dry) properties using Biot-Gassmann relations [*Gassmann*, 1951]:

$$K_u = K_d + \frac{K_f\left(1-\frac{K_d}{K_S}\right)^2}{\Phi + \left(\left(1-\frac{K_d}{K_S}\right)-\Phi\right)\frac{K_f}{K_S}} \quad \text{and} \quad G_u = G_d, \tag{20}$$

where K_d and G_d are, respectively, the drained bulk modulus and shear modulus, Φ the porosity, K_f the saturating fluid's bulk modulus, K_S the skeleton bulk modulus, and K_u and G_u, respectively, the undrained bulk modulus and shear modulus. The Biot-Gassmann predictions for the bulk modulus with water- and glycerin-saturated conditions are presented in Figure 13a, using the parameters K_d = 15 GPa, Φ = 23%,

21699356, 2017, 4, Downloaded from https://agupubs.onlinelibrary.wiley.com/doi/10.1002/2016JB013816 by Cochrane France, Wiley Online Library on [08/02/2023]. See the Terms and Conditions (https://onlinelibrary.wiley.com/terms-and-conditions) on Wiley Online Library for rules of use; OA articles are governed by the applicable Creative Commons License

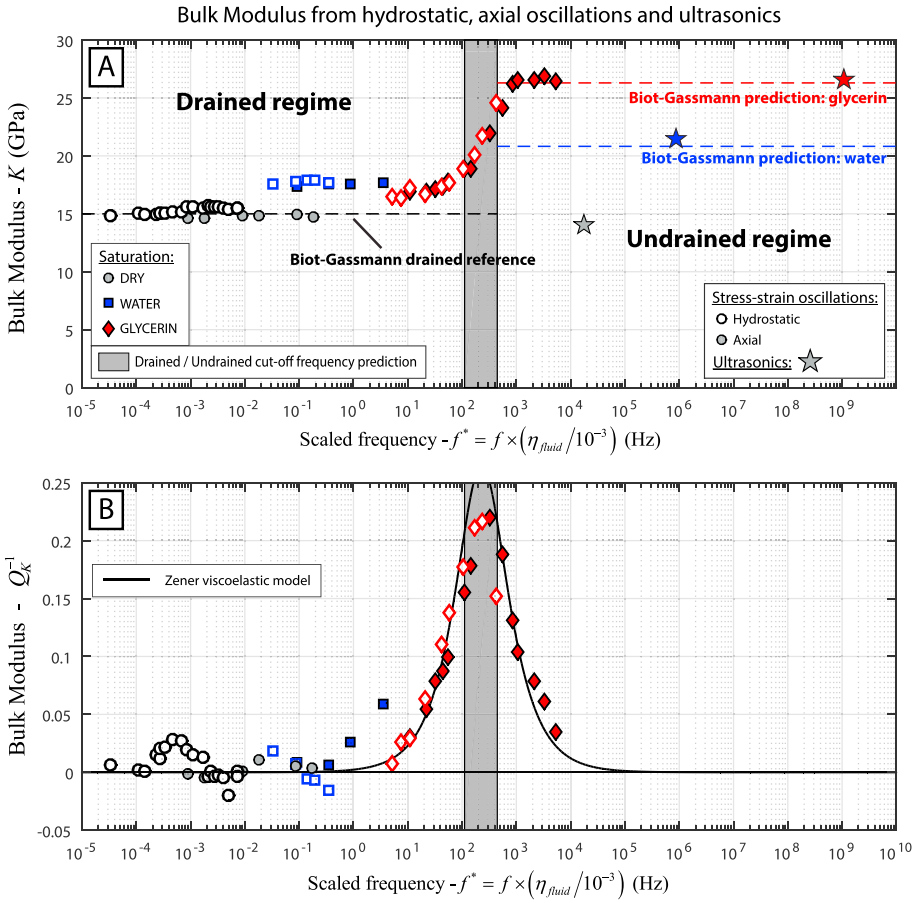

Figure 13. (a) Comparison of the hydrostatic, the axial, and the ultrasonic measurements for the bulk modulus and (b) the bulk modulus Q^{-1} factor deduced from the hydrostatic and axial oscillations for dry-, water-, and glycerin-saturated conditions at $P_{diff} = 2.5$ MPa. Biot-Gassmann's predictions for water and glycerin are represented for the undrained regime in addition to the ultrasonic results (Figure 13a). The frequency is scaled with the viscosities of the saturating fluids.

$K_{f-water} = 2.21$ GPa, $K_{f-glycerin} = 4.36$ GPa [*Bridgman*, 1931], and $K_S = 77$ GPa, which is the bulk modulus of calcite [*Mavko et al.*, 2009]. The predictions give an undrained bulk modulus with water of $K_{u-wat} = 20.8$ GPa and with glycerin $K_{u-gly} = 25.8$ GPa. These results are consistent with the bulk modulus results independently obtained from the stress-strain oscillations under glycerin-saturated conditions (Figure 13a). Moreover, the shear modulus G_{ax} deduced from the axial oscillations is constant over the frequency range of the drained/undrained transition (Figure 10c), which is again consistent with Biot-Gassmann's theory.

5.1.2. Q^{-1} Factors

The Zener viscoelastic model (Figure 3), used to calculate Q^{-1} from the modulus' dispersion, gives accurate results for the Young's modulus (Figure 9b), the bulk modulus (Figures 10b and 11b), and the shear modulus (Figure 10d). However, the model seems to overpredict Q^{-1} for the Poisson's ratio (Figure 9d), with a peak value of 0.13 instead of 0.09. These results, added to similar observations in Fontainebleau sandstones [*Pimienta et al.*, 2015a], show the general good applicability of Zener's model to the drained/undrained transition.

In an isotropic medium, we previously showed that the bulk modulus and the shear modulus can be deduced from axial solicitations and that the bulk modulus gives consistent results with the hydrostatic measurements in the drained and undrained regimes. Therefore, the axial oscillations allow to measure all the moduli if we measure the axial and radial strains. The Young's modulus Q_E^{-1} and Poisson's ratio Q_ν^{-1} are directly measured from the phase shifts between the output signals σ_{ax}, ε_{ax} and ε_{rad} (equation (9)). We presented a method to deduce the bulk modulus $Q_{K_{ax}}^{-1}$ and the shear modulus $Q_{G_{ax}}^{-1}$ from different combinations of the previous output signals (equation (11)). It is therefore of great interest to check the consistency of these Q^{-1} values with existing equations that give relationships between Q^{-1} of all the different moduli. Our aim is to calculate

21699356, 2017, 4, Downloaded from https://agupubs.onlinelibrary.wiley.com/doi/10.1002/2016JB013816 by Cochrane France, Wiley Online Library on [08/02/2023]. See the Terms and Conditions (https://onlinelibrary.wiley.com/terms-and-conditions) on Wiley Online Library for rules of use; OA articles are governed by the applicable Creative Commons License

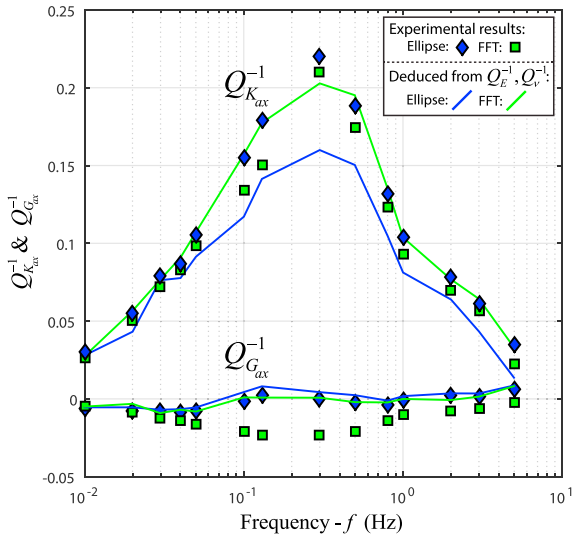

Figure 14. Comparison between $Q_{K_{ax}}^{-1}$ and $Q_{G_{ax}}^{-1}$ obtained experimentally (equation (11)) with the FFT and the Ellipse methods for the drained/undrained transition under glycerin-saturated conditions at $P_{diff} = 2.5$ MPa (Figures 12c and 12d) and the same factors deduced from Q_E^{-1}, Q_ν^{-1}, and ν (equations (22) and (23)).

Q_K^{-1} and Q_G^{-1} from the measured Q_E^{-1} and Q_ν^{-1}. Such relationships have been given by *Winkler and Nur* [1979] but with the hypothesis of a constant Poisson's ratio ν. *Pimienta et al.* [2016c] introduced a dispersive ν into *Winkler and Nur*'s [1979] equations and obtained the following relationship between ν, Q_ν^{-1}, Q_E^{-1}, and Q_G^{-1}:

$$Q_\nu^{-1}\left[\nu + Q_G^{-1}\left((1+\nu)Q_E^{-1} - Q_G^{-1}\right)\right] = (1+\nu)Q_E^{-1} - (1+\nu)Q_G^{-1}. \tag{21}$$

For our purpose, the previous equation can be turned into a second-order polynomial on Q_G^{-1}:

$$-Q_\nu^{-1}\left[Q_G^{-1}\right]^2 + (1+\nu)\left(1 + Q_\nu^{-1}Q_E^{-1}\right)\left[Q_G^{-1}\right] + \left(\nu Q_\nu^{-1} - (1+\nu)Q_E^{-1}\right) = 0, \tag{22}$$

which admits two solutions that can be numerically calculated. The order of magnitudes of these two solutions is around $Q_G^{-1} \sim 0.01$ and $Q_G^{-1} \sim 10$. The second solution being unrealistic as it would give a phase shift between the stress and the strain of nearly $\pi/2$, we keep only the first one. We then calculate the bulk modulus attenuation Q_K^{-1} with the relationship from *Winkler and Nur* [1979]:

$$Q_K^{-1} = \frac{3}{1-2\nu}Q_E^{-1} - \frac{2(1+\nu)}{1-2\nu}Q_G^{-1}. \tag{23}$$

For the axial oscillations, in the frequency range of the drained/undrained transition under glycerin-saturated conditions at $P_{diff} = 2.5$ MPa, the results for Q_K^{-1} and Q_G^{-1} deduced from equations (22) and (23) are reported in Figure 14, along with $Q_{K_{ax}}^{-1}$ and $Q_{G_{ax}}^{-1}$ obtained experimentally from the output signals with the FFT and the Ellipse method (equation (11) and Figures 12c and 12d). The results show a general good match between the two methods to calculate Q_K^{-1} and Q_G^{-1}. Q_K^{-1} as deduced from $Q_{E_{Ellipse}}^{-1}$ and $Q_{\nu_{Ellipse}}^{-1}$ through equations (22) and (23), seems to be a bit lower than the direct experimental result, with a value of 0.15 instead of 0.22 at $f = 0.3$ Hz (Figure 14). This error is solely related to the small difference that was measured between $Q_{\nu_{Ellipse}}^{-1}$ and $Q_{\nu_{FFT}}^{-1}$ (Figure 12b). Note that $Q_{E_{Ellipse}}^{-1} = Q_{E_{FFT}}^{-1}$ (Figure 12a). We can therefore conclude that, in an isotropic medium and for the drained/undrained transition, the axial oscillations allow to measure all moduli and their respective Q^{-1} factors, directly calculated either from σ_{ax}, ε_{ax}, and ε_{rad} (equation (11)) or from the relationships relating ν, Q_E^{-1}, Q_ν^{-1}, Q_K^{-1}, and Q_G^{-1} (equations (22) and (23)).

5.2. Absence of Dispersion at Higher Frequencies

Once the drained and undrained properties of the rock are clearly identified, one can investigate the possible existence of other dispersive transitions at higher frequencies. This concerns a possible unrelaxed (saturated isolated) regime.

21699356, 2017, 4, Downloaded from https://agupubs.onlinelibrary.wiley.com/doi/10.1002/2016JB013816 by Cochrane France, Wiley Online Library on [08/02/2023]. See the Terms and Conditions (https://onlinelibrary.wiley.com/terms-and-conditions) on Wiley Online Library for rules of use; OA articles are governed by the applicable Creative Commons License

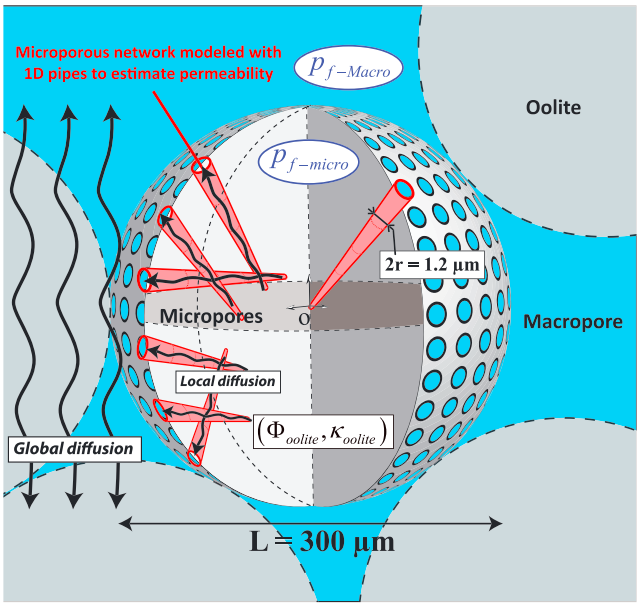

Figure 15. Model of the Lavoux, composed of spherical microporous oolites surrounded by macropores. The global diffusion within the REV and the local diffusion in the oolites are represented. The oolites' porosity (ϕ_{oolite}) is deduced from the experimental total porosity (23%) and from the ratio macroporosity/microporosity (45/55), calculated from the photomicrograph's analysis (Figure 5). A 1-D pipe model (equation (24)) is used to calculate the local permeability of the oolites (κ_{oolite}). The obtained results are $\phi_{oolite} = 14.2\%$ and $\kappa_{oolite} = 1.6 \times 10^{-15}$ m^2. The calculated local permeability of the micropores (κ_{oolite}) is smaller than the sample's permeability measured experimentally ($\kappa = 10^{-14}$ m^2).

5.2.1. No Squirt Flow—Absence of Cracks

Undrained/unrelaxed transitions can exist when local flows occur within the REV in the undrained regime, for instance, squirt flows from compliant cracks to rounded pores [*Mavko and Jizba*, 1991]. The only high-frequency properties available to us in this study are the ultrasonic results (1 MHz) reported Table 1. The high-frequency bulk modulus K_{HF} for dry-, water-, and glycerin-saturated conditions are reported in Figure 13a. In dry conditions, the ultrasonic result corresponds clearly to the drained properties. For water- and glycerin-saturated conditions, the ultrasonic results show a good correspondence with the undrained properties or the Biot-Gassmann's predictions (Figure 13a). We can conclude that no distinct unrelaxed regime is expected beyond the drained/undrained transition for this dual-porosity limestone. In the Lavoux limestone, the elastic moduli are independent of the differential pressure (Figures 7 and 8), suggesting the absence of cracks. Consistently, no squirt flow is thus possible between cracks or from cracks to rounded pores. This is corroborated by the sample's permeability that is also independent of differential pressure (Figure 6) [*Gueguen et al.*, 2011].

5.2.2. No Local Diffusion Between the Microporosity and the Macroporosity

In a bimodal porosity medium, question rises whether there could be a local diffusion between the macroporosity and the microporosity, delayed relative to the global diffusion, due to a lower permeability of the micropores contained in the oolites. The macroporosity of the Lavoux limestone being connected independently of the microporosity, we can model this grainstone as a pile of spherical microporous oolites, of diameters 100 µm to 500 µm, solely surrounded by macropores (Figure 15). The REV of the Lavoux would be a volume containing a few oolites separated by macropores, as no heterogeneity larger than the oolites seems to exist (Figure 4). At $f = 1$ MHz in saturated conditions, the ultrasonic velocities of both the *P* and *S* waves are greater than 1914 m s^{-1} (Table 1) corresponding to a minimum wavelength of approximately 2 mm. This wavelength represents a square area similar to half the area of the photomicrograph presented in Figure 4, containing at least a dozen of oolites. Thus, we can safely assume that, during the propagation of the ultrasonic *P* and *S* waves, the volume of the oscillating stress field is much larger than the limestone's REV. In the undrained regime, the pore pressure is isobaric in the REV [*Gassmann*, 1951], meaning that the fluid's pressure in the macropores ($p_{f-Macro}$) is equal to the fluid's pressure in the oolites' micropores ($p_{f-micro}$) (Figure 15).

Similar to the drained/undrained transition characterized by the cutoff frequency f_1^* that concerns the global fluid flow, a local cutoff frequency $f_{1\ oolite}^*$ could characterize the fluid flow occurring locally from the oolites to

21699356, 2017, 4, Downloaded from https://agupubs.onlinelibrary.wiley.com/doi/10.1002/2016JB013816 by Cochrane France, Wiley Online Library on [08/02/2023]. See the Terms and Conditions (https://onlinelibrary.wiley.com/terms-and-conditions) on Wiley Online Library for rules of use; OA articles are governed by the applicable Creative Commons License

the macropores. The permeability of the oolites κ_{oolite} should be lower than the total permeability of the sample because of a much smaller pore entry radius compared to the macropores (Figure 4). A 1-D permeability model from *Gueguen and Dienes* [1989] can be used to have an estimation of κ_{oolite}. The oolite's microporous network is modeled as a set of pipes of variable radii r and lengths λ, isotropically distributed (Figure 15). If we assume that all the pipes are connected, with respect to the definition of percolation theory, *Gueguen and Dienes* [1989] showed that the permeability of the medium can be given by:

$$\kappa_{\text{oolite}} = \frac{\bar{r}^2}{32}\Phi_{\text{oolite}}. \tag{24}$$

The porosity of the oolite Φ_{oolite} is calculated from the proportion of microporosity in the total porosity, which was deduced from the SEM image analysis at about 55% (Figure 5), and the total porosity measured experimentally at about 23%. If we consider all the microporosity to be in the oolites and the total volume $V_{\text{tot}} = V_{\text{Macropores}} + V_{\text{oolites}}$, we can deduce $\Phi_{\text{oolite}} = 14.2\%$. The average radius $\bar{r}$ is taken as the pore entry radius of the micropores measured from the porosimetry measurements from *Zinsmeister* [2013], and corroborated with the SEM photomicrograph (Figure 4), at about $\bar{r} = 0.6$ µm. Therefore, equation (24) gives a permeability of $\kappa_{\text{oolite}} = 1.6 \times 10^{-15}$ m^2, which is smaller than the sample's global permeability ($\kappa = 10^{-14}$ m^2). Now if we apply the drained/undrained cutoff frequency (equation (1)) to the oolite, with a diffusion length L of about 300µ m (Figure 15) and a drained bulk modulus K_d taken as 15 GPa, we obtain $f^*_{1\,\text{oolite}} = 10^6$ Hz in scaled frequency, which is far above the cutoff frequency of the global diffusion ($f^*_1 = 2 \times 10^2$ Hz). This frequency measures the minimum timescale that allows total diffusion in the oolite and therefore to equilibrate the inner pore pressure $p_{f-\text{micro}}$ and the surrounding pore pressure $p_{f-\text{Macro}}$ (Figure 15). Above $f^*_{1\,\text{oolite}}$, no fluid exchange by diffusion is possible between the oolites and the macropores.

The only measurement we have above $f^*_{1\,\text{oolite}}$ is the ultrasonic measurement in glycerin-saturated conditions ($f^* = 10^9$ Hz). The bulk modulus and shear modulus $K_{\text{HF}-\text{gly}}$ and $G_{\text{HF}-\text{gly}}$ of the sample were found to be equal to their respective undrained values (Table 1 and Figures 10a and 10c). Therefore, no dispersion is visible around $f^*_{1\,\text{oolite}}$, which suggests that there is no flow between the oolites and the macropores in the undrained regime ($f^* > f^*_1$). This is consistent with the idea that the micropores and the macropores have similar aspect ratios ($\xi = 1$), implying no pressure gradients to relax, and that the fluid is isobaric in the REV because the sample is already in the undrained regime. If $f^*_{1\,\text{oolite}}$ had been less than f^*_1, one could imagine a "partially undrained" regime, for a frequency between $f^*_{1\,\text{oolite}}$ and f^*_1, where the oolites are undrained while the macropores are still drained. A local transition around $f^*_{1\,\text{oolite}}$ could then be expected with dispersion and attenuation.

5.3. Effect of the Boundary Conditions — 1-D Diffusion Model for the Drained and Undrained Regimes

The effect of the boundary conditions on the elastic properties has been studied, with two different configurations for the drainage system: (1) open (drained conditions) and (2) closed (undrained conditions for the system sample + dead volumes) (Figure 1a). We recall that all the results presented previously were obtained in the first configuration. Because the dead volumes are very large in that case (∼ 60 mL), the boundary conditions can be assimilated to drained boundary conditions [*Pimienta et al.*, 2016b]. Analogue measurements, using axial and hydrostatic oscillations for a glycerin-saturated sample, have been performed in the closed configuration, with dead volumes of 3.3 mL. The results for the bulk modulus at $P_{\text{diff}} = 2.5$ MPa are reported in Figure 16b, along with the previous results obtained with fully drained conditions (Figure 16a). With dead volumes, the drained/undrained transition is visible around the same cutoff frequency as in the first case, but the dispersion is smaller (Figure 16b). In the drained frequency range, the bulk modulus measured in the second case is higher than in fully drained conditions. Its value is 22 GPa (Figure 16b) instead of 16 GPa (Figure 16a). In the undrained frequency range, the bulk modulus of the sample is independent of the boundary conditions, with a value of 26 GPa in both configurations (Figures 16a and 16b), which is consistent with the definition of the undrained regime.

In the second configuration, the pore pressure in the drainage circuit ($p_f{}^*$) was monitored during the stress oscillations. In order to have a nonzero measurement, $p_f{}^*$ has to be measured in a closed volume to allow for pressure buildup when fluid drains out of the sample. The volumetric strain (ε_{vol}), induced by hydrostatic stress oscillations ($\sigma_{ii}/3$), generates a flux of fluid going in and out of the sample, into the dead volumes. This volumetric strain is defined as follows:

$$\varepsilon_{\text{vol}} = \frac{1}{K}\left(\frac{\sigma_{ii}}{3} - \alpha\Delta p_f\right), \tag{25}$$

21699356, 2017, 4, Downloaded from https://agupubs.onlinelibrary.wiley.com/doi/10.1002/2016JB013816 by Cochrane France, Wiley Online Library on [08/02/2023]. See the Terms and Conditions (https://onlinelibrary.wiley.com/terms-and-conditions) on Wiley Online Library for rules of use; OA articles are governed by the applicable Creative Commons License

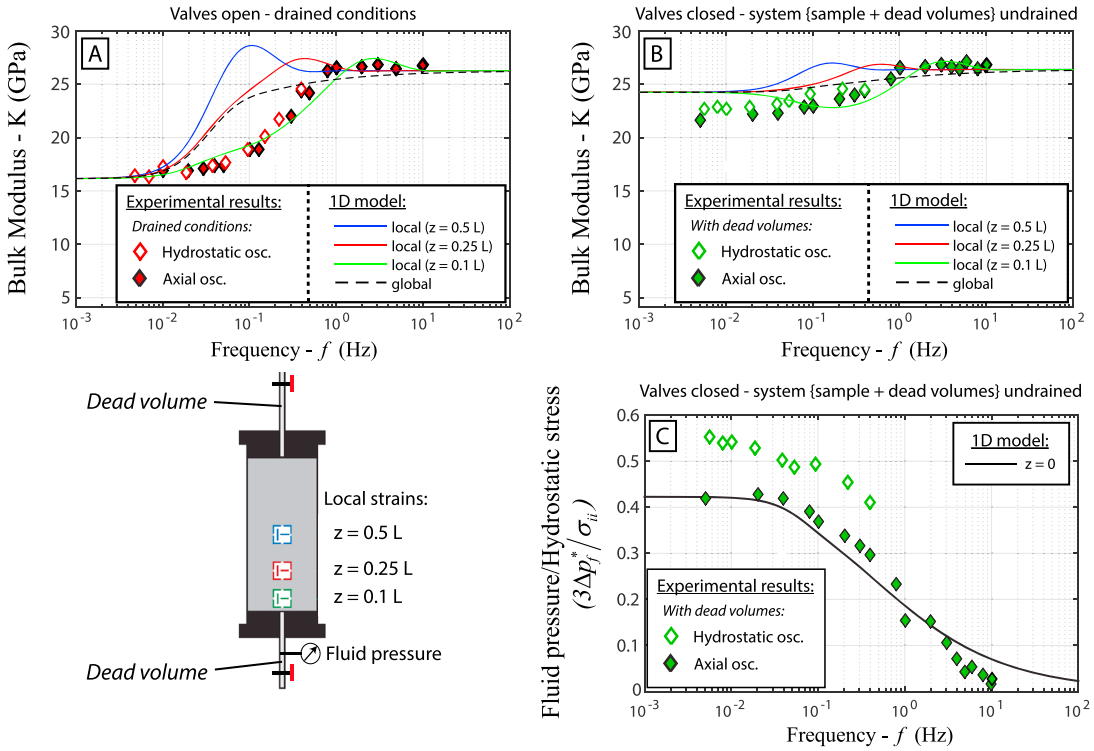

Figure 16. Effect of the two types of experimental boundary conditions on the measured bulk modulus and comparison with the 1-D diffusion model: (a) drained conditions and (b) system sample + dead volumes undrained. The experimental results are from the hydrostatic and axial oscillations in glycerin-saturated conditions at P_{diff} = 2.5 MPa. The model is calculated from local strains at different positions (0.5 *L*, 0.25 *L*, and 0.1 *L*) and from global strain. The experimental results are from strains measured at $z = 0.5\,L$. (c) Measurements of the ratio pore pressure over hydrostatic stress ($3p_f^*/\sigma_{ii}$) in the second type of boundary conditions are compared to the 1-D model, at the limit $z = 0$. For the hydrostatic oscillations $\sigma_{ii}/3 = \Delta P_c$ and for the axial oscillations $\sigma_{ii}/3 = \sigma_{ax}/3$.

where α is the Biot coefficient and Δp_f is the oscillation amplitude of the pore pressure in the medium. Experimentally, when we apply the hydrostatic oscillations on the sample, we have $\sigma_{ii}/3 = \Delta P_c$. This pressure induces the volumetric strain ε_{vol}. On the other hand, when we apply the axial oscillations in an isotropic medium, the equivalent hydrostatic stress to obtain the same volumetric strain ε_{vol} is $\sigma_{ii}/3 = \sigma_{ax}/3$ (equation (25)). Here we assume that the stress σ is positive in compression and represents the amplitude of oscillation and that the radial stress is constant during the axial stress oscillations ($\sigma_{rad} = 0$). For both stress oscillations at $P_{diff} = 2.5$ MPa on glycerin-saturated sample, the ratio between the amplitude of the oscillating fluid pressure $\Delta p_f{}^*$ and the amplitude of the equivalent hydrostatic stress oscillation $\sigma_{ii}/3$ is equal to $3\Delta p_f{}^*/\sigma_{ii}$. This ratio is reported in Figure 16c as a function of frequency. For both hydrostatic and axial oscillations, the ratio tends to zero as the frequency crosses the drained/undrained transition range ($[5 \times 10^{-2}; 1]$ Hz). In the drained frequency range ($f < 5 \times 10^{-2}$ Hz), the ratio measured with hydrostatic measurements is slightly higher than with the axial oscillation, respectively, 0.55 and 0.41 (Figure 16c). This ratio was defined as the "pseudo-Skempton" coefficient $B^* = \Delta p_f{}^*/\Delta P_c$ by *Pimienta et al.* [2015a] in the case of hydrostatic oscillations or the "pseudo-consolidation" parameter $\gamma^* = \Delta p_f{}^*/\sigma_{ax}$ in case of axial oscillations in *Pimienta et al.* [2015b]. This hydraulic parameter cannot be considered as the real Skempton coefficient (*B*) of the sample, because *B* is solely defined for an undrained REV, and $p_f{}^*$ does not measure the pore pressure p_f inside the sample, unless the sample is fully drained.

A 1-D diffusion model has been developed by *Pimienta et al.* [2016b] to take into account these effects of the boundary conditions and has been compared to the previous experimental results (Figure 16). The principle of the model is to find the steady state solution of the diffusion equation for the pore pressure p_f, when the sample undergoes hydrostatic pressure oscillations P_c. Because the lateral surface of the sample is jacketed and the drainage system acts on the top and bottom faces (Figure 1), it was proposed by *Pimienta et al.* [2016b] to solve only the 1-D diffusion along the vertical axis (*z*) of the sample. For the sake of simplicity, $p_f = p_f(z,t) - \bar{p}_f$ and $P_c = P_c(t) - \bar{P}_c$, where $\bar{p}_f$ and $\bar{P}_c$ are the mean pressures during the oscillations, such that $P_{diff} = \bar{P}_c - \bar{p}_f$.

21699356, 2017, 4, Downloaded from https://agupubs.onlinelibrary.wiley.com/doi/10.1002/2016JB013816 by Cochrane France, Wiley Online Library on [08/02/2023]. See the Terms and Conditions (https://onlinelibrary.wiley.com/terms-and-conditions) on Wiley Online Library for rules of use; OA articles are governed by the applicable Creative Commons License

21699356, 2017, 4, Downloaded from https://agupubs.onlinelibrary.wiley.com/doi/10.1002/2016JB013816 by Cochrane France, Wiley Online Library on [08/02/2023]. See the Terms and Conditions (https://onlinelibrary.wiley.com/terms-and-conditions) on Wiley Online Library for rules of use; OA articles are governed by the applicable Creative Commons License

The 1-D diffusion equation writes as follows:

$$\frac{\partial p_f}{\partial t} = \frac{\kappa}{\eta S_s}\frac{\partial^2 p_f}{\partial z^2} + B\frac{\partial P_c}{\partial t}, \tag{26}$$

where S_s is the storage coefficient of the sample, B the Skempton coefficient, and κ the permeability. According to the poroelastic relationships provided by *Kumpel* [1991], $B=(1/K_d-1/K_u)/(1/K_d-1/K_S)$ and $S_s=\alpha/BK_d$. For the model, K_u is deduced from Biot-Gassmann's relationship (equation (20)) to limit the number of adjustment parameters. The applied stress $P_c(t)$ is supposed to be of sinusoidal form such that $P_c(t)=\Delta P_c e^{i\omega t}$. For a sample of length L, *Pimienta et al.* [2016b] give the steady state solution of equation (26) for drained boundary conditions ($p_f(0,t)=p_f(L,t)=0$):

$$p_f(z,t) = B\Delta P_c e^{i\omega t}\left[1-\frac{\sinh(a(L-z))+\sinh(az)}{\sinh(aL)}\right], \tag{27}$$

with $a=(1+i)\sqrt{\omega\eta S_s/2\kappa}$. With symmetric dead volumes on top and bottom of the sample, the solution becomes [*Pimienta et al.*, 2016b]:

$$p_f(z,t) = B\Delta P_c e^{i\omega t}\left[1-\frac{\cosh\left(a\left(\frac{L}{2}-z\right)\right)}{b.\sinh\left(a\frac{L}{2}\right)+\cosh\left(a\frac{L}{2}\right)}\right], \tag{28}$$

with $b=(1-i)A\left(S_s/S\right)\sqrt{2\kappa/\omega\eta S_s}$, A being the cross-sectional area of the sample, and $S=V_{\text{dead vol.}}/K_f$ the storage capacity of the dead volumes. Then, the local volumetric strain is obtained from $\varepsilon_{\text{vol}}(z,t)=K_d{}^{-1}\left(P_c(t)-\alpha p_f(z,t)\right)$, which is a local result. A global volumetric strain can be calculated from $\bar{\varepsilon}_{\text{vol}}(t)=\frac{1}{L}\int_0^L\varepsilon_{\text{vol}}(z,t)\text{d}z$ and can be used to calculate a global bulk modulus. For local or global strain, the bulk modulus is deduced from $K_{model}=-\left|P_c\right|/\left|\bar{\varepsilon}_{\text{vol}}\right|$. Thanks to the model, the ratio fluid pressure over hydrostatic stress ($3p_f/\sigma_{ii}$) could be calculated along the z axis of sample, but for the comparison with the fluid's pressure measured in the dead volumes ($p_f{}^*$), the ratio is evaluated for $z=0$, i.e., $(3p_f{}^*/\sigma_{ii})_{\text{model}}=\left|p_f(0,t)\right|/\left|P_c(t)\right|$. Here we assume that the pore pressure at the boundary is the fluid pressure in the dead volume.

The model's predictions in both configurations for a glycerin-saturated sample are presented in Figure 16. The model has been calculated for local strains at three different positions (0.5 L, 0.25 L, and 0.1 L) and for the global strain. We recall that the experimental results are deduced from local strains measured at $z=0.5\,L$. The parameters used for the model predictions were $L=80$ mm, $A=\pi(40)^2=5027$ mm^2, $K_d=16$ GPa, K_S=77 GPa, $K_f=4.36$ GPa, $\eta=1.083$ Pa s, $\Phi=24\%$, $\kappa=10^{-14}$ m^2, and $V_{\text{dead vol.}}=3.3$ mL. Concerning the bulk modulus in the drained frequency range, the model predicts $K_{\text{model}}=24$ GPa for the second configuration (Figure 16b). This is slightly above the experimental result of 23 GPa (Figure 16b). The bulk modulus K_{model} is 16 GPa in fully drained conditions (Figure 16a). In the undrained frequency range, the model predicts $K_{\text{model}}=26$ GPa (Figure 16a), which by construction of the model corresponds to Biot-Gassmann's prediction. For the ratio $3p_f{}^*/\sigma_{ii}$, the model predicts a value of 0.41 in the drained frequency range, which corresponds to the experimental measurement done with axial oscillations (Figure 16c). For the drained/undrained transition, the ratio $(3p_f{}^*/\sigma_{ii})_{\text{model}}$ decreases down to 0 consistently with the axial experimental results (Figure 16c).

When comparing the model and the experimental results both deduced from local strain at z=0.5 L, we can see a frequency shift of nearly 1 order of magnitude (Figures 16a and 16b). The predicted cutoff frequency is around 0.04 Hz for the model, and the experimental value is 0.2 Hz (Figures 16a and 16b). The model calculated from local strain at $z=0.1\,L$ seems to fit better the experimental results. However, no shift in frequency appears for the ratio $(3p_f{}^*/\sigma_{ii})$ (Figure 16c). The position of the local strain mainly affects the measured cutoff frequency of the transition: the closer to the boundary, the higher the cutoff frequency. In other words, when the frequency of the stress oscillations increases, the REVs at the center of the sample become undrained before the REVs close to the open boundaries. However, the amplitude of the dispersion is unchanged. *Pimienta et al.* [2016b] compared the model to experimental results on Fontainebleau sandstones and found that the cutoff frequency of the bulk modulus was in their case consistent with the experimental results. However, in their case, it was the ratio $3\Delta p_f{}^*/\sigma_{ii}$ that had a frequency shift of 1 order of magnitude compared to the experimental results. Therefore, there seems to be a systematic frequency shift between the bulk modulus and the

21699356, 2017, 4, Downloaded from https://agupubs.onlinelibrary.wiley.com/doi/10.1002/2016JB013816 by Cochrane France, Wiley Online Library on [08/02/2023]. See the Terms and Conditions (https://onlinelibrary.wiley.com/terms-and-conditions) on Wiley Online Library for rules of use; OA articles are governed by the applicable Creative Commons License

ratio $3\Delta p_f^*/\sigma_{ii}$ predicted by the model. This could be due to the limitation to a 1-D diffusion. Experimentally, radial diffusion may occur near the end platens because of the sample's cross section being much larger than the exit holes for the fluid.

6. Conclusion

The elastic moduli (E, ν, K, and G) dispersion and their associated Q^{-1} factors have been measured on a Lavoux limestone, using stress-strain oscillations and ultrasonic measurements in a triaxial cell. The sample was measured under dry-, water-, and glycerin-saturated conditions, which enabled to extend the apparent frequency range of our measurements. Two types of stress oscillations were performed: axial and hydrostatic.

The bulk modulus obtained from both the axial and hydrostatic oscillations compared well over their mutual frequency range, confirming the consistency of both methods when applied on an isotropic material in the drained and undrained regimes. Therefore, the axial oscillations enable to calculate all the moduli and Q^{-1} factors. The formalized relationships between the Q^{-1} factors [*Winkler and Nur*, 1979; *Pimienta et al.*, 2016c] are in agreement with the experimental results, with the condition of a dispersive Poisson's ratio.

The drained/undrained transition has been successfully characterized, with a dispersive effect on all the elastic moduli except for the shear modulus. The Q^{-1} factors were also measured and correlate well with the measured dispersions. The dispersion on K and G is consistent with Biot-Gassmann's theory, either in the water-saturated sample or the glycerin-saturated sample. Experimentally, the boundary conditions around the sample were either drained or undrained for the system sample + dead volumes. A 1-D diffusion model was used to successfully take into account the effect of these boundary conditions on the measured drained moduli.

No other dispersive transitions are detected above the drained/undrained cutoff frequency. We interpret this as an absence of squirt flow due to the absence of cracks. This is corroborated by the fact that the elastic properties and the permeability are independent of effective pressure. We conclude that both the intragranular micropores and intergranular macropores are rounded pores ($\xi_{\text{Macro}} = \xi_{\text{micro}} = 1$). The sample has a bimodal porosity distribution. Local diffusion between the oolites' micropores and the surrounding macropores is however faster than the global diffusion. In other words, the cutoff frequency of the global flow (drained/undrained transition) f_1^* is lower than the theoretical cutoff frequency of the local flow in the oolites $f^*_{1\ \text{oolite}}$.

The drained/undrained transition is measurable in the laboratory. Its critical frequency concerns a global diffusion process on a small length scale, which in our case is the size of the sample L. In the field, with seismic or sonic logs, the global diffusion process would occur within the scale of the wavelength, which is far larger than L for frequencies under 10^5 Hz. Therefore, at the seismic and sonic frequencies, the medium would always be in the undrained regime and be nondispersive. This would not be the case if an open, or drained, boundary condition would exist, for example, a permeable fault.

Acknowledgments
The authors wish to thank D. Deldicque for his expertise on SEM photomicrographs. The authors would also like to thank L. Adam and I. Jackson for their constructive comments. This work has been supported by TOTAL, under project FR00007429. We would like to thank TOTAL for allowing publication of these results. The data for this paper are available by contacting the corresponding author at borgomano@geologie.ens.fr.

References

Adam, L., M. Batzle, and I. Brevik (2006), Gassmann's fluid substitution and shear modulus variability in carbonates at laboratory seismic and ultrasonic frequencies, *Geophysics*, *71*(6), F173–F183, doi:10.1190/1.2358494.

Adam, L., M. Batzle, K. T. Lewallen, and K. van Wijk (2009), Seismic wave attenuation in carbonates, *J. Geophys. Res.*, *114*, B06208, doi:10.1029/2008JB005890.

Adelinet, M., J. Fortin, Y. Guéguen, A. Schubnel, and L. Geoffroy (2010), Frequency and fluid effects on elastic properties of basalt: Experimental investigations, *Geophys. Res. Lett.*, *37*, L02303, doi:10.1029/2009GL041660.

Adelinet, M., J. Fortin, and Y. Gueguen (2011), Dispersion of elastic moduli in a porous-cracked rock: Theoretical predictions for squirt-flow, *Tectonophysics*, *503*(1-2), 173–181, doi:10.1016/j.tecto.2010.10.012.

Anselmetti, F. S., and G. P. Eberli (1993), Controls on sonic velocity in carbonates, *Pure Appl. Geophys.*, *141*(2-4), 287–323.

Baechle, G. T., G. P. Eberli, R. J. Weger, and J. L. Massaferro (2009), Changes in dynamic shear moduli of carbonate rocks with fluid substitution, *Geophysics*, *74*(3), E135–E147, doi:10.1190/1.3111063.

Batzle, M. L., D.-H. Han, and R. Hofmann (2006), Fluid mobility and frequency-dependent seismic velocity—Direct measurements, *Geophysics*, *71*(1), N1–N9.

Bemer, E., and J. Lombard (2010), From injectivity to integrity studies of CO_2 geological storage: Chemical alteration effects on carbonates petrophysical and geomechanical properties, *Oil Gas Sci. Technol. – Revue de l'Inst. Francais du Pet.*, *65*(3), 445–459, doi:10.2516/ogst/2009028.

Bosart, L., and A. Snoddy (1927), New glycerol tables, *Ind. Eng. Chem.*, *19*(4), 506–510.

Bridgman, P. W. (1931), The volume of eighteen liquids as a function of pressure and temperature, *Proc. Am. Acad. Arts Sci.*, *66*(5), 185–233, doi:10.2307/20026332.

Clark, V. A., B. R. Tittmann, and T. W. Spencer (1980), Effect of volatiles on attenuation (Q^{-1}) and velocity in sedimentary rocks, *J. Geophys. Res.*, *85*(B10), 5190–5198, doi:10.1029/JB085iB10p05190.

Cleary, M. P. (1978), Elastic and dynamic response regimes of fluid-impregnated solids with diverse microstructures, *Int. J. Solids Struct.*, *14*(10), 795–819, doi:10.1016/0020-7683(78)90072-0.
David, E. C., J. Fortin, A. Schubnel, Y. Gueguen, and R. W. Zimmerman (2013), Laboratory measurements of low-and high-frequency elastic moduli in Fontainebleau sandstone, *Geophysics*, *78*(5), D369–D379.
Dvorkin, J., G. Mavko, and A. Nur (1995), Squirt flow in fully saturated rocks, *Geophysics*, *60*(1), 97–107, doi:10.1190/1.1443767.
Eberli, G. P., G. T. Baechle, F. S. Anselmetti, and M. L. Incze (2003), Factors controlling elastic properties in carbonate sediments and rocks, *Leading Edge*, *22*(7), 654–660.
Fabre, D., and J. Gustkiewicz (1997), Poroelastic properties of limestones and sandstones under hydrostatic conditions, *Int. J. Rock Mech. Min. Sci.*, *34*(1), 127–134, doi:10.1016/S1365-1609(97)80038-X.
Fabricius, I. L., G. T. Bächle, and G. P. Eberli (2010), Elastic moduli of dry and water-saturated carbonates—Effect of depositional texture, porosity, and permeability, *Geophysics*, *75*(3), N65–N78, doi:10.1190/1.3374690.
Fortin, J., A. Schubnel, and Y. Gueguen (2005), Elastic wave velocities and permeability evolution during compaction of Bleurswiller sandstone, *Int. J. Rock Mech. Min. Sci.*, *42*(7-8), 873–889, doi:10.1016/j.ijrmms.2005.05.002.
Fortin, J., L. Pimienta, Y. Guéguen, A. Schubnel, E. C. David, and M. Adelinet (2014), Experimental results on the combined effects of frequency and pressure on the dispersion of elastic waves in porous rocks, *Leading Edge*, *33*(6), 648–654.
Fournier, F., and J. Borgomano (2009), Critical porosity and elastic properties of microporous mixed carbonate-siliciclastic rocks, *Geophysics*, *74*(2), E93–E109, doi:10.1190/1.3043727.
Gassmann, F. (1951), Elasticity of porous media, *Vierteljahrsschrder Naturforschenden Gesselschaft*, *96*, 1–23.
Gueguen, Y., and J. Dienes (1989), Transport properties of rocks from statistics and percolation, *Math. Geol.*, *21*(1), 1–13.
Gueguen, Y., M. Adelinet, A. Ougier-Simonin, J. Fortin, and A. Schubnel (2011), How cracks modify permeability and introduce velocity dispersion: Examples of glass and basalt, *Leading Edge*, *30*(12), 1392–1398.
Kumpel, H.-J. (1991), Poroelasticity: Parameters reviewed, *Geophys. J. Int.*, *105*(3), 783–799, doi:10.1111/j.1365-246X.1991.tb00813.x.
Lucia, F. J. (1995), Rock-fabric/petrophysical classification of carbonate pore space for reservoir characterization, *Am. Assoc. Pet. Geol. Bull.*, *79*(9), 1275–1300.
Madonna, C., and N. Tisato (2013), A new seismic wave attenuation module to experimentally measure low-frequency attenuation in extensional mode, *Geophys. Prospect.*, *61*(2), 302–314.
Mavko, G., and D. Jizba (1991), Estimating grain-scale fluid effects on velocity dispersion in rocks, *Geophysics*, *56*(12), 1940–1949, doi:10.1190/1.1443005.
Mavko, G., T. Mukerji, and J. Dvorkin (2009), *The Rock Physics Handbook: Tools for Seismic Analysis of Porous Media*, 460 pp., Cambridge Univ. Press, Cambridge, U. K.
Mikhaltsevitch, V., M. Lebedev, and B. Gurevich (2014), A laboratory study of low-frequency wave dispersion and attenuation in water-saturated sandstones, *Leading Edge*, *33*(6), 616–622.
Mikhaltsevitch, V., M. Lebedev, and B. Gurevich (2016a), Laboratory measurements of the effect of fluid saturation on elastic properties of carbonates at seismic frequencies: Effect of fluid saturation on carbonates, *Geophys. Prospect.*, *64*(4), 799–809, doi:10.1111/1365-2478.12404.
Mikhaltsevitch, V., M. Lebedev, and B. Gurevich (2016b), Validation of the laboratory measurements at seismic frequencies using the Kramers-Kronig relationship, *Geophys. Res. Lett.*, *43*, 4986–4991, doi:10.1002/2016GL069269.
Muller, T. M., B. Gurevich, and M. Lebedev (2010), Seismic wave attenuation and dispersion resulting from wave-induced flow in porous rocks—A review, *Geophysics*, *75*(5), 75A147–75A164.
O'Connell, R. J., and B. Budiansky (1977), Viscoelastic properties of fluid-saturated cracked solids, *J. Geophys. Res.*, *82*(36), 5719–5735, doi:10.1029/JB082i036p05719.
O'Connell, R. J., and B. Budiansky (1978), Measures of dissipation in viscoelastic media, *Geophys. Res. Lett.*, *5*(1), 5–8, doi:10.1029/GL005i001p00005.
O'Donnell, M., E. Jaynes, and J. Miller (1981), Kramers-Kronig relationship between ultrasonic attenuation and phase velocity, *J. Acoust. Soc. Am.*, *69*(3), 696–701.
Pimienta, L., J. Fortin, and Y. Gueguen (2014), Investigation of elastic weakening in limestone and sandstone samples from moisture adsorption, *Geophys. J. Int.*, *199*(1), 335–347, doi:10.1093/gji/ggu257.
Pimienta, L., J. Fortin, and Y. Gueguen (2015a), Bulk modulus dispersion and attenuation in sandstones, *Geophysics*, *80*(2), D111–D127, doi:10.1190/geo2014-0335.1.
Pimienta, L., J. Fortin, and Y. Gueguen (2015b), Experimental study of Young's modulus dispersion and attenuation in fully saturated sandstones, *Geophysics*, *80*(5), L57–L72, doi:10.1190/geo2014-0532.1.
Pimienta, L., J. Fortin, J. V. M. Borgomano, and Y. Gueguen (2016a), Dispersions and attenuations in a fully saturated sandstone: Experimental evidence for fluid flows at different scales, *Leading Edge*, *35*(6), 495–501, doi:10.1190/tle35060495.1.
Pimienta, L., J. V. M. Borgomano, J. Fortin, and Y. Gueguen (2016b), Modelling the drained/undrained transition: Effect of the measuring method and the boundary conditions: Modelling drained/undrained transition, *Geophys. Prospect.*, *64*(4), 1098–1111, doi:10.1111/1365-2478.12390.
Pimienta, L., J. Fortin, and Y. Gueguen (2016c), Effect of fluids and frequencies on Poisson's ratio of sandstone samples, *Geophysics*, *81*(2), D183–D195, doi:10.1190/geo2015-0310.1.
Rasolofosaon, P., and B. Zinszner (2002), Vérification expérimentale de la formule de Gassmann dans les calcaires poreux, *Oil Gas Sci. Technol.*, *57*(2), 129–138.
Sarout, J. (2012), Impact of pore space topology on permeability, cut-off frequencies and validity of wave propagation theories: Pore space topology and wave propagation, *Geophys. J. Int.*, *189*(1), 481–492, doi:10.1111/j.1365-246X.2011.05329.x.
Segur, J. B., and H. E. Oberstar (1951), Viscosity of glycerol and its aqueous solutions, *Ind. Eng. Chem.*, *43*(9), 2117–2120, doi:10.1021/ie50501a040.
Shafiro, B., and M. Kachanov (1997), Materials with fluid-filled pores of various shapes: Effective elastic properties and fluid pressure polarization, *Int. J. Solids Struct.*, *34*(27), 3517–3540, doi:10.1016/S0020-7683(96)00185-0.
Spencer, J. W., and J. Shine (2016), Seismic wave attenuation and modulus dispersion in sandstones, *Geophysics*, *81*(3), D211–D231, doi:10.1190/geo2015-0342.1.
Szewczyk, D., A. Bauer, and R. M. Holt (2016), A new laboratory apparatus for the measurement of seismic dispersion under deviatoric stress conditions: Apparatus for seismic dispersion, *Geophys. Prospect.*, *64*(4), 789–798, doi:10.1111/1365-2478.12425.
Tisato, N., and C. Madonna (2012), Attenuation at low seismic frequencies in partially saturated rocks: Measurements and description of a new apparatus, *J. Appl. Geophys.*, *86*, 44–53, doi:10.1016/j.jappgeo.2012.07.008.

21699356, 2017, 4, Downloaded from https://agupubs.onlinelibrary.wiley.com/doi/10.1002/2016JB013816 by Cochrane France, Wiley Online Library on [08/02/2023]. See the Terms and Conditions (https://onlinelibrary.wiley.com/terms-and-conditions) on Wiley Online Library for rules of use; OA articles are governed by the applicable Creative Commons License

Verwer, K., G. Eberli, G. Baechle, and R. Weger (2010), Effect of carbonate pore structure on dynamic shear moduli, *Geophysics*, *75*(1), E1–E8, doi:10.1190/1.3280225.

Vincent, B., M. Fleury, Y. Santerre, and B. Brigaud (2011), NMR relaxation of neritic carbonates: An integrated petrophysical and petrographical approach, *J. Appl. Geophys.*, *74*(1), 38–58, doi:10.1016/j.jappgeo.2011.03.002.

Winkler, K., and A. Nur (1979), Pore fluids and seismic attenuation in rocks, *Geophys. Res. Lett.*, *6*(1), 1–4, doi:10.1029/GL006i001p00001.

Winkler, K. W., and W. F. Murphy (1995), Acoustic velocity and attenuation in porous rocks, in *Rock Physics and Phase Relations: A Handbook of Physical Constants*, pp. 20–34, AGU, Washington, D. C.

Youssef, S., M. Han, D. Bauer, E. Rosenberg, S. Bekri, M. Fleury, and O. Vizika (2008), High resolution µCT combined to numerical models to assess electrical properties of bimodal carbonates, UAE, Abu Dhabi, 29 Oct.–2 Nov.

Zinsmeister, L. (2013), Study of the hydromechanical evolution of a carbonate after chemical alteration. Application of the 2D and 3D digital image correlation during mechanical loading at different scales, Thesis, Ecole Polytechnique X, Palaiseau, France. [Available at https://pastel.archives-ouvertes.fr/pastel-00955351.]

21699356, 2017, 4, Downloaded from https://agupubs.onlinelibrary.wiley.com/doi/10.1002/2016JB013816 by Cochrane France, Wiley Online Library on [08/02/2023]. See the Terms and Conditions (https://onlinelibrary.wiley.com/terms-and-conditions) on Wiley Online Library for rules of use; OA articles are governed by the applicable Creative Commons License